


 Cite this: *RSC Adv.*, 2025, 15, 29571

# Microwave-assisted co-precipitation synthesis of $MFe_2O_4$ nanoferrites ( $M = Co$ and $Mn$ ) using biogenic coir extract and their physical characterization

 Tran Thi Ngoc Nha,<sup>a</sup> Sankar Hari Prakash,<sup>b</sup> Selvaraj Mohana Roopan,<sup>b</sup> James Jebaseelan Samuel,<sup>c</sup> Dang Ngoc Toan,<sup>d,e</sup> Dinh Thanh Khan,<sup>f</sup> Do Danh Bich,<sup>g</sup> Tran Dang Thanh,<sup>h</sup> Le Thi Tuyet Ngan,<sup>i</sup> Do Hung Manh<sup>h</sup> and Pham Thanh Phong<sup>\*,j,k</sup>

$MFe_2O_4$  ( $M = Co$  and  $Mn$ ) nanoparticles were synthesized from coconut coir extract using a microwave-assisted co-precipitation method, representing a green and sustainable approach for ferrite nanomaterial preparation. The physical properties of the samples were characterized using X-ray diffraction, scanning electron microscopy, ultraviolet-visible spectroscopy, photoluminescence, Raman spectroscopy, and vibrating sample magnetometry. Scanning electron micrographs revealed nanoscale morphology with evidence of polymorphism. Rietveld refinement confirmed the formation of single-phase spinel ferrites with lattice constants ranging from 8.4224 Å to 8.4782 Å for  $CoFe_2O_4$  and  $MnFe_2O_4$ , respectively. The distribution of metal cations at the tetrahedral and octahedral sites in the  $AB_2O_4$  spinel lattice was found to depend on the synthesis route and significantly influenced the magnetic and optical behaviors of the materials. Raman spectra exhibited characteristic peaks corresponding to a mixed spinel structure. The optical band gaps estimated from the UV-vis spectra were 2.66 eV for  $CoFe_2O_4$  and 2.64 eV for  $MnFe_2O_4$ . PL spectra showed four distinct emission peaks at 458, 692, 758, and 871 nm. Based on UV-vis and photoluminescence spectral results, a schematic energy band structure was constructed. Magnetic measurements, analyzed using the “law of approach” to saturation, revealed saturation magnetizations of 70  $emu\ g^{-1}$  ( $CoFe_2O_4$ ) and 49  $emu\ g^{-1}$  ( $MnFe_2O_4$ ) at 55 K—values that are among the highest reported for these systems; the squareness ratios were 0.58 and 0.12, respectively. The  $CoFe_2O_4$  sample exhibited high effective anisotropy due to surface spin contributions, resulting in high coercivity and squareness. In contrast, the enhanced dipolar interactions in  $MnFe_2O_4$  reduced coercivity and squareness. These magnetic behaviors were interpreted within the frameworks of the Stoner–Wohlfarth and superparamagnetic models that account for interparticle interactions.

 Received 9th July 2025  
 Accepted 7th August 2025

DOI: 10.1039/d5ra04897d

[rsc.li/rsc-advances](http://rsc.li/rsc-advances)

## 1. Introduction

Spinel ferrites ( $MFe_2O_4$ ;  $M = Co, Mn, Ni, Zn, etc.$ ) with cubic crystal structures have garnered significant attention for

applications in engineering and biomedical fields.<sup>1</sup> At the nanoscale, these materials are particularly attractive for use in biomedicine, environmental treatment, and photocatalytic processes, including water splitting and pollutant degradation.<sup>2</sup>

<sup>a</sup>Graduate University of Science and Technology, Vietnam Academy of Science and Technology, 18 Hoang Quoc Viet, Hanoi, Vietnam

<sup>b</sup>Chemistry of Heterocycles & Natural Product Research Laboratory, Department of Chemistry, School of Advanced Sciences, Vellore Institute of Technology, Vellore, Tamil Nadu, India

<sup>c</sup>Medical Gel Dosimetry Lab, Department of Physics, School of Advanced Sciences, Vellore Institute of Technology, Vellore, Tamil Nadu, India

<sup>d</sup>Institute of Research and Development, Duy Tan University, Danang 550000, Vietnam

<sup>e</sup>Faculty of Natural Sciences, Duy Tan University, Danang 550000, Vietnam

<sup>f</sup>The University of Danang-University of Science and Education, Danang 550000, Vietnam

<sup>g</sup>Faculty of Physics, Hanoi National University of Education, 136 Xuan Thuy, Cau Giay, Hanoi 100000, Vietnam

<sup>h</sup>Institute of Materials Science, Vietnam Academy of Science and Technology, 18 Hoang Quoc Viet, Hanoi, Vietnam

<sup>i</sup>Faculty of Engineering and Technology, Thai Nguyen University of Information and Communication Technology, Z115 Street, Quyet Thang Ward, Thai Nguyen Province, Vietnam

<sup>j</sup>Laboratory of Magnetism and Magnetic Materials, Science and Technology Advanced Institute, Van Lang University, Ho Chi Minh City, Vietnam. E-mail: phamthanhphong@vlu.edu.vn

<sup>k</sup>Faculty of Applied Technology, School of Technology, Van Lang University, Ho Chi Minh City, Vietnam


The spinel structure consists of a cubic close-packed array of 32 oxygen anions, with 24 metal cations distributed across two distinct crystallographic sites: tetrahedral (A) and octahedral (B) interstices.<sup>3</sup> Depending on the preferential site occupancy of metal ions, spinel ferrites are classified as normal, inverse, or mixed (partially inverted) spinels. In a normal spinel, divalent metal ions ( $M^{2+}$ ) occupy the A sites, while trivalent iron ions ( $Fe^{3+}$ ) are situated at the B sites. In contrast, an inverse spinel structure features  $Fe^{3+}$  ions equally divided between the A and B sites, with all  $M^{2+}$  ions occupying the B sites. In a mixed/partially inverted spinel structure, the distribution of  $M^{2+}$  and  $Fe^{3+}$  ions across the A and B sublattices is completely random. Therefore, the general chemical formula for  $MFe_2O_4$  spinels can be expressed as  $(M_{1-x}^{2+}Fe_x^{3+})[M_x^{2+}Fe_{2-x}^{3+}]O_4^{2-}$ , where parentheses and square brackets denote the A and B sites, respectively, and  $x$  represents the fraction of  $Fe^{3+}$  ions occupying the A sublattice.<sup>4</sup> Because the net magnetic moment in spinel ferrites originates from superexchange interactions between the A and B sublattices,<sup>5</sup> variations in  $x$  significantly influence the magnetic properties. Moreover, nanostructured ferrites typically exhibit distinct microstructural and magnetic characteristics compared to their bulk counterparts.<sup>6</sup> At the nanoscale, fluctuations in  $x$  can be substantial due to size-dependent effects, leading to ion redistribution within the spinel lattice. Consequently, the magnetic behavior of ferrite nanocrystals is governed not only by quantum confinement effects—as seen in other nanomaterials—but also by specific cation distributions. Among the various ferrites,  $CoFe_2O_4$  and  $MnFe_2O_4$  have emerged as particularly promising materials owing to their versatility in a wide range of technological applications.<sup>7,8</sup>

Manganese ferrite ( $MnFe_2O_4$ ) in its bulk form is generally classified as a normal spinel<sup>9</sup> or, in some cases, a mixed spinel.<sup>10</sup> However, at the nanoscale,  $MnFe_2O_4$  nanoparticles (NPs) typically exhibit a mixed or partially inverted spinel structure, which can be described by the formula  $(Mn_{1-x}^{2+}Fe_x^{3+})[Mn_x^{2+}Fe_{2-x}^{3+}]O_4^{2-}$ .<sup>4</sup> This cation redistribution enhances the strength of the superexchange interactions between the A and B sublattices, potentially resulting in a higher saturation magnetization compared to their bulk counterparts.<sup>9</sup> These distinctive structural and magnetic features render  $MnFe_2O_4$ -based nanoparticles highly suitable for a range of applications, including magnetic data storage, catalysis, ferrofluids, sensors, and actuators.<sup>11</sup> Furthermore,  $MnFe_2O_4$  NPs have demonstrated significant promise in magneto-optical and optoelectronic devices due to their capability to absorb low-energy photons, making them ideal for photocatalytic applications.<sup>12,13</sup> Their inherently low coercivity, high magnetic permeability, and minimal energy loss also position them as attractive candidates for biomedical technologies, such as targeted drug delivery, magnetic hyperthermia, and magnetic resonance imaging contrast enhancement.<sup>14,15</sup>

In contrast, cobalt ferrite ( $CoFe_2O_4$ ) exhibits an inverse spinel structure in its bulk form, a configuration that is largely preserved even at the nanoscale.<sup>16</sup>  $CoFe_2O_4$  NPs are characterized by a high Curie temperature ( $T_C \approx 793$  K), large coercivity, moderate saturation magnetization ( $\sim 80$  emu  $g^{-1}$  at room temperature), and pronounced magnetocrystalline anisotropy.

In addition, they possess exceptional chemical and electrochemical stability, high mechanical hardness, and excellent magnetic permeability.<sup>17</sup> These properties have enabled their deployment across a diverse array of biomedical and technological domains, including antibacterial, anticancer, antioxidant, and enzyme-inhibitory applications, as well as in energy storage systems, catalytic processes, and components for sensors, transistors, solar cells, and photocatalytic devices.<sup>18–23</sup>

The diverse applications of ferrites necessitate the selection of appropriate synthesis techniques to ensure optimal performance. A variety of physical and chemical methods have been employed for the fabrication of ferrite NPs, including sol-gel,<sup>24</sup> hydrothermal,<sup>25</sup> co-precipitation,<sup>26</sup> thermal decomposition,<sup>27</sup> and high-energy ball milling.<sup>28</sup> While these approaches offer flexibility in process control and enable the rapid production of large quantities of ferrite NPs, many rely on the use of toxic solvents, reducing agents, and stabilizers. Such chemicals pose significant environmental and health hazards, especially in long-term exposure. Consequently, there is an increasing demand for alternative, environmentally benign synthesis routes—particularly green methodologies—that minimize toxic by-products while maintaining or enhancing the desired functional properties of nanoferrites.

Among the various techniques, co-precipitation is widely favored due to its simplicity and capacity for precise control over key synthesis parameters, such as particle size, morphology, temperature, pH, precursor concentration, and alkali addition rate.<sup>29</sup> However, achieving high crystallinity in the resulting ferrite NPs typically requires a post-synthesis calcination step at elevated temperatures.<sup>30</sup> Moreover, maintaining consistent product quality and stability throughout the synthesis process can be challenging, particularly when the precipitation reaction lacks continuous control.<sup>31</sup> To address these limitations, we propose a green, microwave-assisted co-precipitation method that incorporates a biocompatible and non-toxic natural surfactant derived from coconut coir extract. This approach integrates the advantages of microwave heating with sustainable synthesis practices. Microwave irradiation significantly reduces reaction time and enhances reaction efficiency by directly coupling with materials through mechanisms, such as dielectric and magnetic interactions, in contrast to the indirect convective heating used in conventional methods.<sup>25,32</sup> As a result, this method facilitates rapid and uniform heating of reactants, promotes homogeneous nucleation, and enables the formation of well-defined, crystalline  $MFe_2O_4$  nanoparticles. The proposed technique thus represents a promising, eco-friendly strategy for the synthesis of high-performance ferrite nanomaterials.

$MFe_2O_4$  ( $M = Co, Mn, Ni, Zn, etc.$ ) NPs have been successfully synthesized using phytochemicals extracted from various plant components, including flowers, leaves, stems, seeds, fruits, and roots.<sup>33</sup> These biological sources, often derived from agricultural waste or naturally occurring plants, are typically washed with distilled water to remove surface impurities. The extracts are then obtained either directly from fresh biomass or through drying and grinding processes. Among these sources, coconut stands out as one of the most abundant and readily available



plants in Southeast Asia and India, making it an ideal candidate for synthesizing green nanomaterials. In particular, coconut-coir extract has been shown to contain various phytochemicals, such as polyphenols, tannins, and flavonoids, which act as natural reducing and stabilizing agents during the formation of nanoparticles.<sup>34</sup> These compounds facilitate the formation of metal oxide nanoparticles by reducing metal ions and preventing agglomeration, thereby enabling a sustainable and non-toxic synthesis route. The reducing capability of these phytochemicals has been previously verified using FTIR spectroscopy. For example, Elango *et al.*<sup>35,36</sup> reported the disappearance or shift of the -OH and C=O stretching bands after the synthesis of Ni and Pd nanoparticles with coconut coir extract, suggesting that these functional groups are directly involved in the redox reaction. Although our current study did not include FTIR or LC-MS analysis, the presence of such functional groups in the extract—as confirmed in earlier studies—strongly supports its role in nanoparticle formation. The effective control over particle size and phase purity observed in our work is thus consistent with the phytochemical-mediated synthesis mechanism proposed in the literature. Despite its availability, only a limited number of studies have employed coconut-based bioextracts in the synthesis of nanoparticle formulations. Existing reports have focused primarily on the green synthesis of metal and metal oxide nanoparticles—such as silver, lead, palladium, copper oxide, and zinc oxide—using coconut coir as a reducing and stabilizing agent.<sup>34–38</sup> To date, however, no reports have been published on the one-step green synthesis of CoFe<sub>2</sub>O<sub>4</sub> and MnFe<sub>2</sub>O<sub>4</sub> NPs *via* microwave-assisted co-precipitation (MAP) using coconut coir extract. The present study addresses this gap by developing a sustainable MAP approach for the synthesis of MFe<sub>2</sub>O<sub>4</sub> (M = Co, Mn) NPs. We further investigate the influence of morphology, crystal structure, and cation distribution on the optical and magnetic properties of the resulting materials. In particular, the UV-vis absorption data were used to estimate the optical bandgap, while photoluminescence (PL) measurements supported the construction of energy band structure diagrams. These spectral results also allowed us to assess the photo-thermal response of the samples using theoretical parameters derived from Mie theory. Beyond the novelty of the green synthesis approach, this work reveals notable differences in the magnetic behavior between CoFe<sub>2</sub>O<sub>4</sub> and MnFe<sub>2</sub>O<sub>4</sub> NPs. While the magnetism in CoFe<sub>2</sub>O<sub>4</sub> is predominantly governed by surface spin contributions, the magnetic properties of MnFe<sub>2</sub>O<sub>4</sub> are better described by a modified superparamagnetic interaction model.

Importantly, the synthesis process described here does not require external catalysts, is performed at ambient temperature and atmospheric pressure, and relies entirely on non-toxic, plant-derived materials—highlighting its potential for eco-friendly and scalable production of functional ferrite nanomaterials. Unlike previous reports that use either microwave heating or plant extracts separately, this study uniquely combines both, with coconut-coir extract serving as the biogenic complexing agent—an approach not yet reported in the literature for transition-metal ferrites.

## 2. Experimental

### 2.1. Fabrication of MFe<sub>2</sub>O<sub>4</sub> (M = Co and Mn) NPs

**2.1.1. Materials.** Cobalt(II) chloride hexahydrate (CoCl<sub>2</sub>·6H<sub>2</sub>O, 98%; Avra, India), manganese(II) chloride (MnCl<sub>2</sub>, 98%; Aldrich, USA), anhydrous iron(III) chloride (FeCl<sub>3</sub>, 98%; Avra, India), citric acid monohydrate (C<sub>6</sub>H<sub>8</sub>O<sub>7</sub>·H<sub>2</sub>O, 99.7–102%; Himedia, India), and sodium hydroxide (NaOH, 97%; Molychem, India) were used as precursors without further purification. Coconut coir was sourced from the local market in Vellore, India. Distilled water and ethanol were used throughout the synthesis process.

**2.1.2. Preparation of coconut coir extract.** Coconut coir (*Cocos nucifera*) was thoroughly washed with distilled water to remove dust and surface impurities, followed by air-drying at room temperature. A total of 10 g of the dried coir was then mixed with 100 mL of distilled water and heated at ~60 °C for 30 minutes to enhance extraction efficiency. The resulting mixture was filtered using a sterile cheesecloth to obtain a clear aqueous extract, which was used directly in the nanoparticle synthesis. The remaining extract was stored at 4 °C in a refrigerator for subsequent use. This preparation method ensured consistent phytochemical composition and maximized the utilization of the coconut coir biomass.<sup>34</sup>

**2.1.3. Synthesis of MFe<sub>2</sub>O<sub>4</sub> (M = Co and Mn) NPs.** MFe<sub>2</sub>O<sub>4</sub> (M = Co, Mn) nanoparticles were synthesized *via* a microwave-assisted co-precipitation method. Stoichiometric amounts of M<sup>2+</sup> and Fe<sup>3+</sup> precursors were dissolved in 35 mL of distilled water at a molar ratio of 1 : 2 under continuous magnetic stirring. The pH of the solution was adjusted to approximately 10 by the dropwise addition of 50 mL of 1 M NaOH solution to initiate the co-precipitation process. Subsequently, 20 mL of coconut coir extract was added as a biogenic stabilizing agent. The resulting mixture was transferred to a microwave reactor (SINEO UWave-1000 Microwave Ultraviolet Ultrasonic Synthesis/Extraction Reactor) and irradiated at 350 W for 30 minutes. After completion, the reaction vessel was allowed to cool naturally to room temperature under ambient conditions. During this stage, the pH gradually decreased and stabilized near neutral. The resulting black precipitate was separated by centrifugation, washed repeatedly with distilled water and ethanol to remove unreacted residues and by-products, and then dried in a hot-air oven at 80 °C for 4 hours to obtain the final ferrite nanopowder.

### 2.2. Characterization of MFe<sub>2</sub>O<sub>4</sub> (M = Co and Mn) NPs

The crystal structure and phase purity of the synthesized MFe<sub>2</sub>O<sub>4</sub> nanoparticles were analyzed using an X-ray diffractometer (Bruker D8 ADVANCE Eco) with Cu K $\alpha$  radiation ( $\lambda = 0.154$  nm) over a  $2\theta$  range of 10° to 80°, with a scanning step size of 0.02°. Rietveld refinement was performed using FullProf software employing a Lorentz profile function to extract the lattice parameters and cation distributions across the tetrahedral (A) and octahedral (B) sites. The surface morphology and particle size were examined using a scanning electron microscope (SEM, Hitachi S-4800), which was also equipped with an



energy-dispersive X-ray spectroscopy (EDX) detector to determine the elemental composition of the samples. Optical band gap values were determined from UV-vis absorption spectra recorded on a JASCO V-770 UV-vis spectrophotometer. PL measurements were carried out using a Horiba Fluorolog 3 FL3-22 spectrofluorometer with an excitation wavelength of 310 nm. Raman spectra were acquired using a Horiba XploRA PLUS Micro Raman spectrometer with a 785 nm laser excitation source. Magnetic properties were assessed by measuring hysteresis loops at room temperature using a Quantum Design VersaLab Physical Property Measurement System (model VL173), under an applied magnetic field of up to 30 kOe.

In this study, samples were fabricated at Vellore Institute of Technology, India. The X-ray diffraction (XRD), Raman, and PL measurements were conducted at the University of Science and Education, Danang University. The SEM and magnetic measurements were performed at the Institute of Materials Science, Vietnam Academy of Science and Technology, and UV-vis measurements were conducted at Hanoi National University of Education.

### 3. Results and discussion

#### 3.1. Structural studies of $MFe_2O_4$ NPs

Fig. 1(a and b) present the X-ray diffraction (XRD) patterns of  $CoFe_2O_4$  and  $MnFe_2O_4$  NPs. All observed diffraction peaks are in good agreement with the standard reference patterns from the Crystallography Open Database (COD), specifically card no. 153-5820 for  $CoFe_2O_4$  and card no. 230-0585 for  $MnFe_2O_4$ . These patterns confirm the formation of single-phase spinel structures with space group  $Fd\bar{3}m$ , characteristic of ferrite systems.

Within the detection limits of the XRD measurements, no impurity phases or residual precursor signals were detected, indicating high phase purity.

Furthermore, the reproducibility of the synthesis protocol was evaluated by repeating the microwave-assisted synthesis under the same fixed conditions (power, time, and precursor concentration). The resulting XRD patterns showed negligible variation across batches, confirming the robustness of the protocol for both  $CoFe_2O_4$  and  $MnFe_2O_4$  ferrites. Although the *in situ* monitoring of pH or temperature was not conducted, the consistent phase formation across multiple experiments indicates that the reaction proceeds reliably once the optimal conditions are established. This observation is consistent with prior reports that employed fixed microwave parameters to achieve reproducible spinel ferrite phases without the need for kinetic monitoring.<sup>39–41</sup>

To obtain precise crystallographic information, Rietveld refinement was performed using the FullProf software suite. The fitted profiles (red lines) exhibit excellent agreement with the experimental data (black dots), as shown in Fig. 1(a and b). The refinement quality was quantitatively assessed using the goodness-of-fit parameter ( $\chi^2$ ), calculated from the final weighted profile ( $R_{wp}$ ) and expected  $R$ -factor ( $R_{Exp}$ ). In general, if  $\chi^2$  lies within the reliability criterion of  $1 \leq \chi^2 < 2$  or  $R_{wp}$  is less than 10%, refinement can be considered to be of a high degree of refinement accuracy.<sup>42</sup>

It is worth noting that the reduced  $\chi^2$  value obtained from the Rietveld refinement is relatively low (see Table 1), approximately 0.035. Although values in the range  $1 < \chi^2 < 2$  are often considered typical, significantly lower values may occur when the dataset has very low statistical variance—particularly in

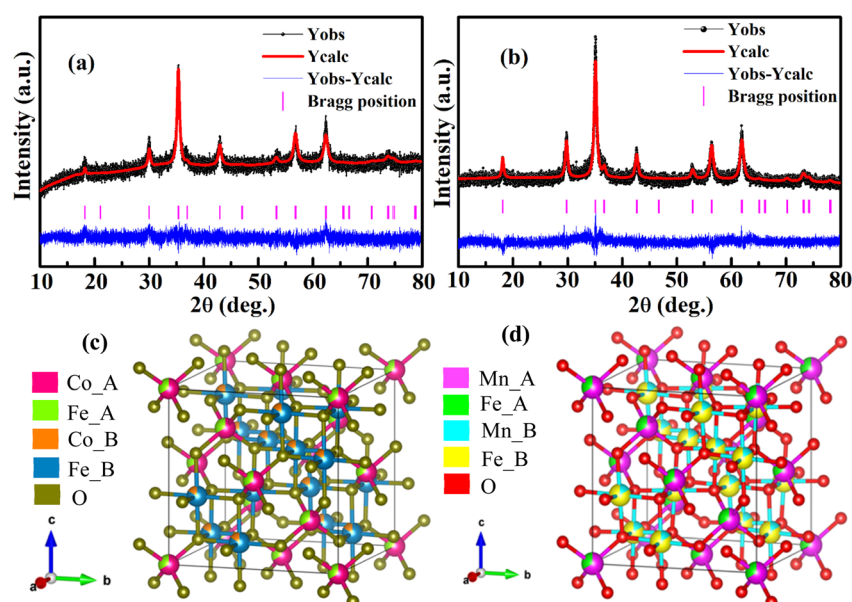


Fig. 1 XRD patterns and Rietveld refinement profiles of (a)  $CoFe_2O_4$  and (b)  $MnFe_2O_4$ . (c and d) Three-dimensional representations of the refined crystal structures of  $CoFe_2O_4$  and  $MnFe_2O_4$ , respectively, constructed using structural parameters obtained from Rietveld analysis. The spinel framework illustrates the tetrahedral (A) and octahedral (B) sites, where the cation distributions—Co\_A (Mn\_A), Co\_B (Mn\_B), Fe\_A, and Fe\_B—are denoted. The relative occupancy percentages of metal cations at A and B sites are represented by the corresponding-colored segments of the spheres.



**Table 1** Cation distribution, experimental lattice parameter ( $a_{\text{exp}}$ ), unit cell volume ( $V$ ), profile factor ( $R_p$ ), weighted factor ( $R_{\text{wp}}$ ), goodness factor ( $\chi^2$ ), crystalline grain diameter ( $D$ ), strain ( $\epsilon$ ) and grain size ( $d$ ) of  $\text{MFe}_2\text{O}_4$  nanoparticles

Sample	Cation distribution		$a_{\text{exp}}$ (Å)	$V$ (Å <sup>3</sup> )	$R_p$ (%)	$R_{\text{wp}}$ (%)	$\chi^2$	$D$ (nm)	$\epsilon$ ( $10^{-3}$ )	$d$ (nm)
	A site	B site								
$\text{CoFe}_2\text{O}_4$	$\text{Co}_{0.658}^{2+}\text{Fe}_{0.342}^{3+}$	$\text{Co}_{0.342}^{2+}\text{Fe}_{1.658}^{3+}$	8.4224	597.45	5.94	7.54	0.035	15.74	0.52	17.21
$\text{MnFe}_2\text{O}_4$	$\text{Mn}_{0.670}^{2+}\text{Fe}_{0.330}^{3+}$	$\text{Mn}_{0.330}^{2+}\text{Fe}_{1.670}^{3+}$	8.4782	609.41	8.06	10.3	0.029	29.51	2.48	29.83

cases of high-quality experimental data, low background noise, and a large number of refined points. As discussed by Brian H. Toby,<sup>42</sup> such conditions can reduce the denominator of the  $\chi^2$  equation (*i.e.*, the variance of the intensity), thereby lowering the overall value without implying overfitting or an artificially perfect model. This interpretation is consistent with our results: the difference plot ( $Y_{\text{obs.}} - Y_{\text{calc.}}$ ) shown in Fig. 1 exhibits random, non-systematic deviations around zero, further confirming the validity of the model. Additionally, the refinement achieved  $R_{\text{wp}}$  values below 10%, which—together with the low  $\chi^2$ —provides strong evidence for the reliability and consistency of the extracted structural parameters within the spinel phase.

The experimentally determined lattice parameters ( $a_{\text{exp}}$ ) and unit cell volumes are listed in Table 1. These values are consistent with those reported in prior studies on spinel ferrite systems.<sup>4,6,43,44</sup> Notably, the lattice parameter of  $\text{MnFe}_2\text{O}_4$  was found to be larger than that of  $\text{CoFe}_2\text{O}_4$ . This difference can be attributed to the larger ionic radii of  $\text{Mn}^{2+}$  ions compared to  $\text{Co}^{2+}$  ions at both tetrahedral (A) and octahedral (B) sites (0.66 Å vs. 0.58 Å at A sites; 0.83 Å vs. 0.745 Å at B sites),<sup>45</sup> resulting in a greater lattice expansion for  $\text{MnFe}_2\text{O}_4$ . In addition to lattice constants, the cation distribution in the spinel lattice was estimated from Rietveld refinement using a crystallographic model constrained by the  $Fd\bar{3}m$  space group symmetry. Although conventional XRD lacks the sensitivity to unambiguously distinguish between transition metal cations with similar atomic numbers (*e.g.*,  $\text{Co}^{2+}$ ,  $\text{Mn}^{2+}$ ,  $\text{Fe}^{3+}$ ), the refinement provides semi-quantitative insight into site occupancies when constrained by physically meaningful structural models. The obtained inversion parameters for  $\text{CoFe}_2\text{O}_4$  and  $\text{MnFe}_2\text{O}_4$  are consistent with literature values reported for materials synthesized under comparable conditions.<sup>46</sup> The reliability of the refinement is supported by low  $R_{\text{wp}}$  and  $\chi^2$  values, as well as by well-distributed residual plots (Fig. 1), indicating good agreement between the experimental and calculated diffraction profiles.

While more element-specific techniques such as Mössbauer spectroscopy or X-ray absorption spectroscopy (XAS) are typically required for a definitive determination of site occupancies, the present refinement yields values that are in good agreement with those obtained from such methods in previous studies.<sup>47–49</sup> Accordingly, the cation distributions discussed herein should be regarded as refined estimations based on structural constraints rather than absolute determinations. The refined site occupancies and atomic coordinates are summarized in Table 1, and the corresponding crystallographic models are illustrated in Fig. 1(c and d). For  $\text{CoFe}_2\text{O}_4$ , the tetrahedral 8a site

was occupied by 34%  $\text{Co}^{2+}$  and 66%  $\text{Fe}^{3+}$ , while the octahedral 16d site was composed of 17%  $\text{Co}^{2+}$  and 83%  $\text{Fe}^{3+}$ . In the case of  $\text{MnFe}_2\text{O}_4$ , the 8a site was occupied by 33%  $\text{Mn}^{2+}$  and 67%  $\text{Fe}^{3+}$ , whereas the 16d site was composed of 32%  $\text{Mn}^{2+}$  and 68%  $\text{Fe}^{3+}$ . In both samples, the oxygen anions fully occupied the 32e site. The observed distribution of  $\text{M}^{2+}$  and  $\text{Fe}^{3+}$  ions across both tetrahedral and octahedral sites confirms the formation of mixed spinel structures in  $\text{CoFe}_2\text{O}_4$  and  $\text{MnFe}_2\text{O}_4$  nanoparticles. This cationic disorder is known to significantly influence the magnetic and optical properties of spinel ferrites and is consistent with the results reported in the literature.

Based on the Rietveld refinement results, the full width at half maximum (FWHM) values for all diffraction peaks in the XRD patterns of  $\text{CoFe}_2\text{O}_4$  and  $\text{MnFe}_2\text{O}_4$  nanoparticles were determined and subsequently used to estimate the average crystallite size and lattice strain through Williamson–Hall (W–H) analysis. The W–H equation is expressed as:

$$\beta_{hkl} \cos \theta = \left( \frac{K\lambda}{D} \right) + (4\epsilon \sin \theta), \quad (1)$$

where  $\beta_{hkl}$  is the peak broadening (FWHM) after correction for instrumental broadening,  $\theta$  is the Bragg angle,  $K$  is the shape factor (typically 0.9),  $D$  (in nm) is the average crystallite size,  $\epsilon$  is the lattice strain, and  $\lambda$  (0.154 nm) is the X-ray wavelength.

Fig. 2 illustrates the W–H plots of  $\beta_{hkl} \cos \theta$  versus  $4\epsilon \sin \theta$  for both  $\text{CoFe}_2\text{O}_4$  and  $\text{MnFe}_2\text{O}_4$  samples. The fitted linear trends follow eqn (1), with the slope corresponding to the lattice strain and the  $Y$ -intercept (at  $\sin \theta = 0$ ) was used to calculate the average crystallite size. As summarized in Table 1, the estimated average crystallite sizes were 15.7 nm for  $\text{CoFe}_2\text{O}_4$  and 29.5 nm for  $\text{MnFe}_2\text{O}_4$ . Interestingly, the lattice strain was found to increase from  $0.52 \times 10^{-3}$  in  $\text{CoFe}_2\text{O}_4$  to  $2.48 \times 10^{-3}$  in  $\text{MnFe}_2\text{O}_4$ , despite the concurrent increase in crystallite size. This behavior contrasts with the typical inverse relationship between crystallite size and lattice strain, where smaller crystallites tend to exhibit higher strain due to enhanced lattice distortion at reduced dimensions.<sup>50</sup> In this case, however, the trend reversal is attributed to the larger ionic radius of  $\text{Mn}^{2+}$  compared to  $\text{Co}^{2+}$ , which leads to an expansion of lattice constant and unit cell volume, thereby increasing internal strain within the crystal lattice.<sup>51,52</sup>

An increase in crystallite size was generally accompanied by an increase in particle size, as revealed by the field-emission scanning electron microscopy (FE-SEM) images presented in Fig. 3(a and c). In these images, the  $\text{MFe}_2\text{O}_4$  nanoparticles were observed to form nearly spherical morphologies with relatively uniform sizes, although some extent of agglomeration was also



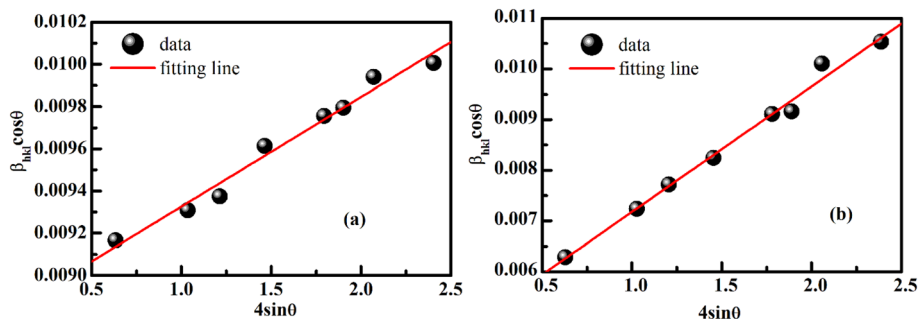


Fig. 2 Williamson–Hall (W–H) plots for (a)  $\text{CoFe}_2\text{O}_4$  and (b)  $\text{MnFe}_2\text{O}_4$  nanoparticles. The red lines represent linear fits to the experimental data based on the W–H equation. The lattice strain was calculated from the slope of the fitted line, while the average crystallite size was determined from the y-intercept.

evident. Particle size distribution histograms, constructed using ImageJ software and shown in the inset of Fig. 3(a and c), were employed to statistically determine the average particle diameters ( $d$ ) of the samples.

As summarized in Table 1, the mean particle size was found to increase from 17.21 nm for  $\text{CoFe}_2\text{O}_4$  to 29.83 nm for  $\text{MnFe}_2\text{O}_4$ . This difference may be attributed to the variation in ionic radii between  $\text{Mn}^{2+}$  and  $\text{Co}^{2+}$  ions, which are known to affect the crystallization dynamics and grain growth rates

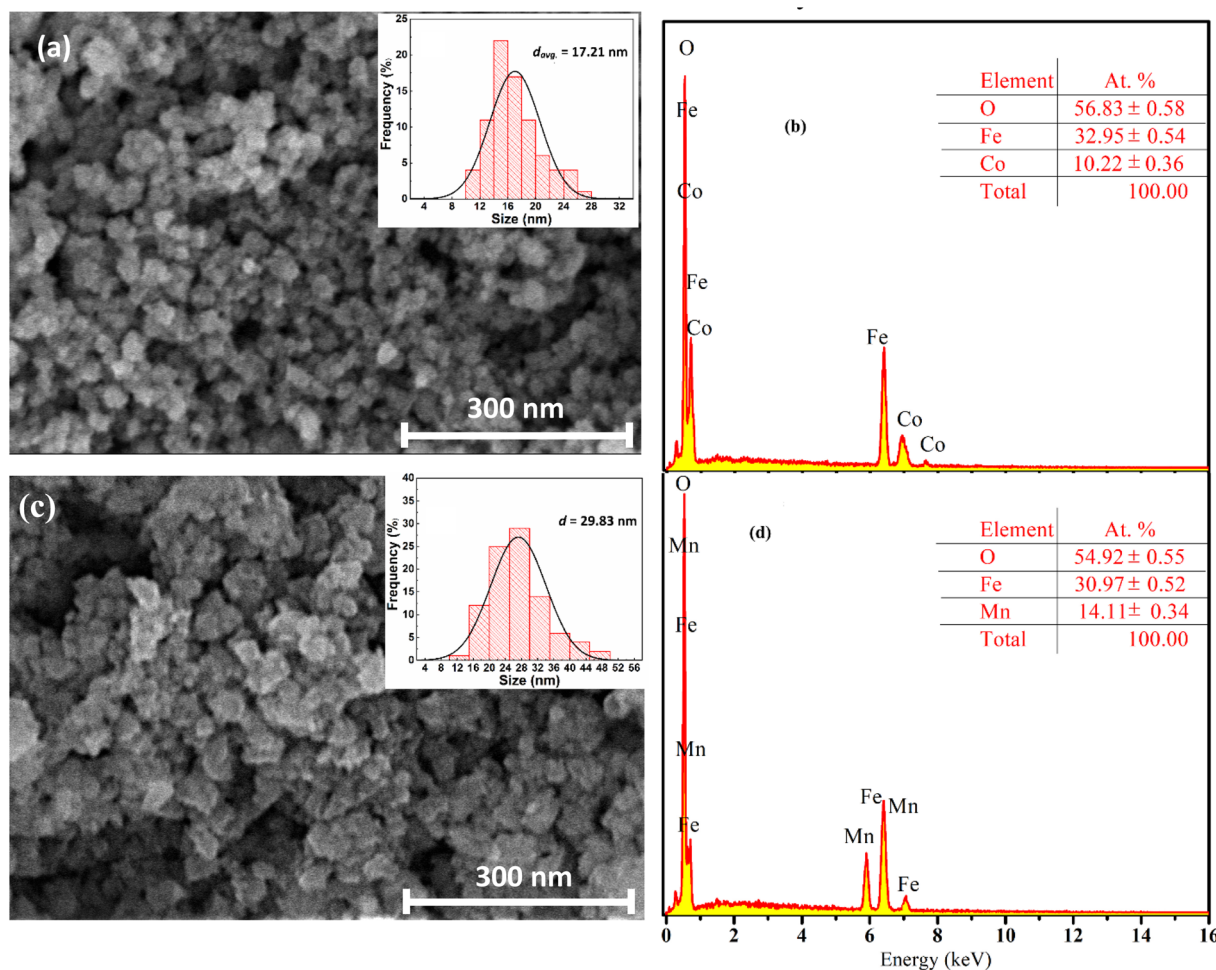


Fig. 3 Field-emission scanning electron microscopy (FE-SEM) images and energy-dispersive X-ray (EDX) spectra of (a and c)  $\text{CoFe}_2\text{O}_4$  and (b and d)  $\text{MnFe}_2\text{O}_4$  nanoparticles. The insets of (a) and (c) show the corresponding particle size distribution histograms, derived from the FE-SEM images using ImageJ software. The insets of (b) and (d) display the elemental compositions obtained from EDX analysis, indicating the atomic percentages of metal cations and oxygen anions at representative positions on each sample.



during synthesis. The grain sizes estimated from SEM analysis were found to be in close agreement with the crystallite sizes obtained from X-ray diffraction (XRD) using the Williamson–Hall method, with minimal deviation. This consistency suggests that the particles are likely to be monocrystalline or consist of highly crystalline domains. Furthermore, no sub-grain boundaries or distinct contrast variations were observed within individual particles in the SEM micrographs, which would otherwise indicate internal polycrystallinity. Although the possibility of inter-crystallite agglomeration cannot be entirely excluded, the absence of inter-particle fringes, combined with the close correspondence to the XRD-derived sizes, supports the assumption that the grains are structurally coherent and predominantly single-domain. Nevertheless, it is acknowledged that more conclusive identification of crystallinity would require high-resolution transmission electron microscopy (HRTEM) or selected area electron diffraction (SAED), which were beyond the scope of the current study.

As shown in the insets of Fig. 3(b and d), the atomic percentages of metal cations and anions, determined from the EDX spectra averaged over three different positions for each sample, were found to be close to the ideal cation-to-anion stoichiometric ratio of 3:4 for spinel ferrites. This observation further confirmed that the metal precursors were effectively incorporated into the ferrite lattice, forming compositionally homogeneous  $M\text{Fe}_2\text{O}_4$  nanoparticles without detectable residual or impurity elements.

In addition, the lattice strain ( $\epsilon$ ), determined *via* Williamson–Hall analysis, was found to increase from  $0.52 \times 10^{-3}$  for  $\text{CoFe}_2\text{O}_4$  to  $2.48 \times 10^{-3}$  for  $\text{MnFe}_2\text{O}_4$ . This trend indicates that the incorporation of Mn ions not only expanded the unit cell but also introduced greater internal stress, which could further influence both the microstructural evolution and the functional properties of the materials.

### 3.2. Raman spectroscopic analysis of $\text{MFe}_2\text{O}_4$ NPs

Micro-Raman spectroscopy is a powerful tool for probing the microstructural and vibrational characteristics of both bulk and

nanoscale materials.<sup>53</sup> It provides insight into the lattice dynamics by measuring the Raman-active vibrational modes associated with atomic or molecular displacements within a material. For spinel ferrites with a partially or fully inverted structure and belonging to the  $Fd\bar{3}m$  space group, group theory predicts five Raman-active modes:  $A_{1g} + E_g + 3T_{2g}$ . Among these, the  $T_{2g}$  modes are typically designated as  $T_{2g}(1)$ ,  $T_{2g}(2)$ , and  $T_{2g}(3)$ , with increasing frequency. In many cases, only the most intense modes— $A_{1g}$ ,  $T_{2g}(2)$ , and  $T_{2g}(3)$ —are clearly observed in experimental spectra. Typically, the  $A_{1g}$  mode appears in the range of  $570\text{--}780\text{ cm}^{-1}$  and corresponds to the symmetric stretching of oxygen with respect to the metal cation at the tetrahedral (A) site. The  $T_{2g}(3)$  and  $T_{2g}(2)$  modes are generally located at  $\sim 450\text{--}500\text{ cm}^{-1}$  and  $\sim 350\text{--}400\text{ cm}^{-1}$ , respectively, while the lower-frequency  $E_g$  and  $T_{2g}(1)$  modes may appear below  $300\text{ cm}^{-1}$ , depending on instrument sensitivity and sample crystallinity.<sup>54</sup>

Fig. 4 displays the Raman spectra of  $\text{CoFe}_2\text{O}_4$  and  $\text{MnFe}_2\text{O}_4$  nanoparticles, recorded in the spectral range of  $70\text{--}1000\text{ cm}^{-1}$ . Peak assignment was performed based on literature ref. 55–59. The  $A_{1g}$  mode was observed at  $633\text{ cm}^{-1}$  for  $\text{CoFe}_2\text{O}_4$  and  $672\text{ cm}^{-1}$  for  $\text{MnFe}_2\text{O}_4$ , attributed to the symmetric stretching vibration of oxygen atoms in the  $\text{AO}_4$  tetrahedra. The  $T_{2g}(3)$ ,  $T_{2g}(2)$ , and  $T_{2g}(1)$  modes, corresponding to various symmetric and asymmetric bending vibrations of the metal–oxygen bonds, were observed at approximately  $480$ ,  $304$ , and  $125\text{ cm}^{-1}$  for  $\text{CoFe}_2\text{O}_4$  and at  $459$ ,  $308$ , and  $125\text{ cm}^{-1}$  for  $\text{MnFe}_2\text{O}_4$ , respectively. Most of the Raman bands appeared asymmetric, indicating overlapping vibrational contributions from multiple lattice sites. To resolve these overlapping features, spectral deconvolution was performed. The fitting parameters obtained are summarized in Table 2. The presence of multiple sub-peaks, often represented as doublets,<sup>16,57–59</sup> further supports the existence of a mixed or partially inverted spinel structure in both samples, consistent with previous reports. This splitting of Raman modes can be attributed to variations in cation occupancy between tetrahedral (A) and octahedral (B) sites, leading to local symmetry distortions and non-equivalent vibrational

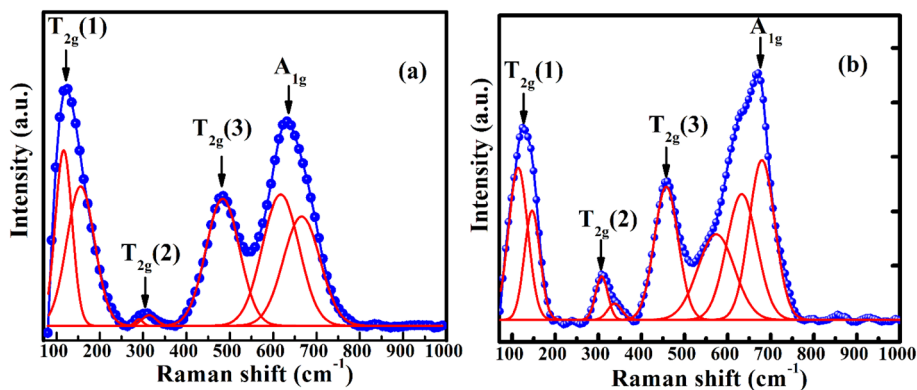


Fig. 4 Raman spectra of  $\text{CoFe}_2\text{O}_4$  (a) and  $\text{MnFe}_2\text{O}_4$  (b) NPs recorded in the range of  $70\text{--}1000\text{ cm}^{-1}$ . The observed peaks correspond to the Raman-active modes predicted for spinel ferrites with  $Fd\bar{3}m$  symmetry. The strong  $A_{1g}$  mode appears at  $633\text{ cm}^{-1}$  and  $672\text{ cm}^{-1}$  for  $\text{CoFe}_2\text{O}_4$  and  $\text{MnFe}_2\text{O}_4$ , respectively, while the  $T_{2g}(3)$ ,  $T_{2g}(2)$ , and  $T_{2g}(1)$  modes are detected at lower frequencies. Peak deconvolution reveals splitting into sub-bands, indicative of cation disorder and mixed or partially inverted spinel structures.

Table 2 Raman vibrational modes for MFe<sub>2</sub>O<sub>4</sub> (M = Co and Mn) nanoparticles

Sample	T <sub>2g</sub> (1) (cm <sup>-1</sup> )	T <sub>2g</sub> (1) (cm <sup>-1</sup> )	T <sub>2g</sub> (2) (cm <sup>-1</sup> )	T <sub>2g</sub> (2) (cm <sup>-1</sup> )	T <sub>2g</sub> (3) (cm <sup>-1</sup> )	T <sub>2g</sub> (3) (cm <sup>-1</sup> )	A <sub>1g</sub> (cm <sup>-1</sup> )	A <sub>1g</sub> (cm <sup>-1</sup> )
CoFe <sub>2</sub> O <sub>4</sub>	117.25(0)	155.33(4)	287.98(5)	310.09(3)	482.62(1)	—	617.33(8)	667.54(7)
MnFe <sub>2</sub> O <sub>4</sub>	80.86(2)	109.78(5)	337.33(4)	413.11(9)	453.70(9)	595.30(1)	619.36(7)	666.88(2)

environments. Such structural disorder, arising from partial inversion and site-sharing between Co<sup>2+</sup> and Fe<sup>3+</sup> ions, directly influences the observed optical phonon modes and results in the complex spectral features recorded. Therefore, the Raman spectra serve as a sensitive probe of the cation distribution and local structural symmetry in the spinel lattice. These findings are consistent with the cation distribution obtained from Rietveld refinement, demonstrating the complementary nature of Raman spectroscopy and crystallographic analysis in elucidating the structural properties of ferrite nanoparticles.

### 3.3. Optical properties and schematic of the electronic band structure for MFe<sub>2</sub>O<sub>4</sub> NPs

The ultraviolet-visible (UV-vis) absorption spectrum serves as a valuable tool for investigating electronic transitions between metal cations at the tetrahedral (A) and octahedral (B) sites within spinel ferrites. Owing to the strong light absorption characteristics of ferrite materials in the UV-visible region, insights into their optical and electronic structures can be obtained from such measurements. Fig. 5 presents the room-temperature UV-vis absorbance spectra of MFe<sub>2</sub>O<sub>4</sub> (M = Co, Mn) NPs, recorded over the 300–800 nm wavelength range. Both samples exhibited broad absorption bands in the 350–600 nm region, which can be attributed to the formation of well-defined spinel crystal structures, magnetic exchange interactions, electronic complexity due to mixed cation occupancy, and quantum size effects.<sup>60</sup> In addition, a weak absorption tail extending beyond 800 nm was observed, suggesting the presence of indirect electronic transitions associated with phonon-assisted electron transfer processes—characteristic of some ferrite systems.<sup>61</sup>

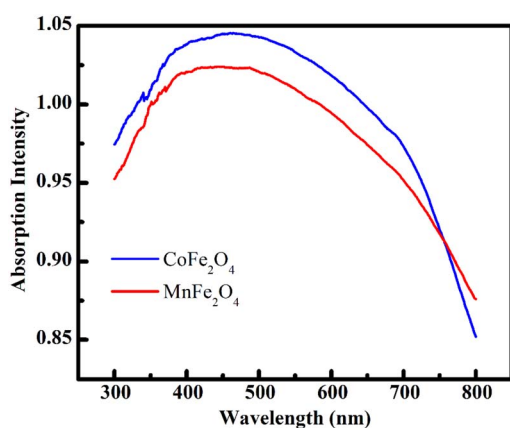


Fig. 5 Optical absorption spectra for the CoFe<sub>2</sub>O<sub>4</sub> and MnFe<sub>2</sub>O<sub>4</sub> nanoparticles.

The optical bandgap energy ( $E_g$ ) of the samples was estimated using the Tauc relation:<sup>62</sup>

$$\alpha hv = A(hv - E_g)^n, \quad (2)$$

where  $\alpha$  is the absorption coefficient,  $hv$  is the incident photon energy,  $A$  is a proportionality constant, and  $n$  is a transition-related exponent. The value of  $n$  indicates the nature of the electronic transition:  $n = 1/2$  for allowed direct,  $n = 2$  for allowed indirect,  $n = 3/2$  for forbidden direct, and  $n = 3$  for forbidden indirect transitions.

In the case of spinel ferrites, such as CoFe<sub>2</sub>O<sub>4</sub> and MnFe<sub>2</sub>O<sub>4</sub>, numerous theoretical and experimental studies have confirmed that they exhibit direct allowed transitions.<sup>63–65</sup> Therefore, the Tauc plots in Fig. 6(a and b) were constructed using  $n = 1/2$ , corresponding to a direct allowed transition, and the optical bandgap was extracted from the linear extrapolation of  $(\alpha hv)^2$  versus  $hv$ .

The  $E_g$  values were determined by extrapolating the linear portion of the plots to the photon energy axis ( $hv$ ), where  $(\alpha hv)^2 = 0$ . The estimated bandgap energies were 2.66 eV for CoFe<sub>2</sub>O<sub>4</sub> and 2.64 eV for MnFe<sub>2</sub>O<sub>4</sub>, in close agreement with previously reported values for similar nanocrystalline ferrites.<sup>64,65</sup> These results confirm that the optical properties of the synthesized nanoparticles are consistent with those expected for spinel-type MFe<sub>2</sub>O<sub>4</sub> materials.

The presence of structural defects in a material introduces localized states within the bandgap, which can significantly alter the electronic band structure by disrupting the long-range periodic potential. These defects impede the direct excitation of electrons into the conduction band and give rise to an exponential absorption tail in the sub-bandgap region of the UV-vis spectrum, commonly known as the “Urbach tail”.<sup>66</sup> The characteristic energy associated with this tail is termed the Urbach energy ( $E_u$ ), which provides a quantitative measure of the degree of structural disorder in a material.<sup>67</sup>

The Urbach energy can be derived from the absorption coefficient ( $\alpha$ ) using the relation:

$$\alpha = \alpha_0 \left[ \sigma \left( \frac{E - E_0}{k_B T} \right) \right], \quad (3)$$

where  $\alpha_0$ ,  $E$ , and  $E_0$  are the absorption coefficient, photon energy, and onset of absorption, respectively. The  $\alpha_0$  and  $E_0$  values depend on the characteristics of each material, and  $E_u = k_B T / \sigma$  is referred to as the Urbach energy, where  $\sigma$  and  $k_B$  are the steepness parameter and the Boltzmann constant, respectively.

Fig. 6(c and d) present the plots of  $\ln(\alpha)$  versus photon energy ( $E$ ) for CoFe<sub>2</sub>O<sub>4</sub> and MnFe<sub>2</sub>O<sub>4</sub> NPs, respectively. The  $E_u$  values, determined from the inverse slopes of the linear fits in the low-



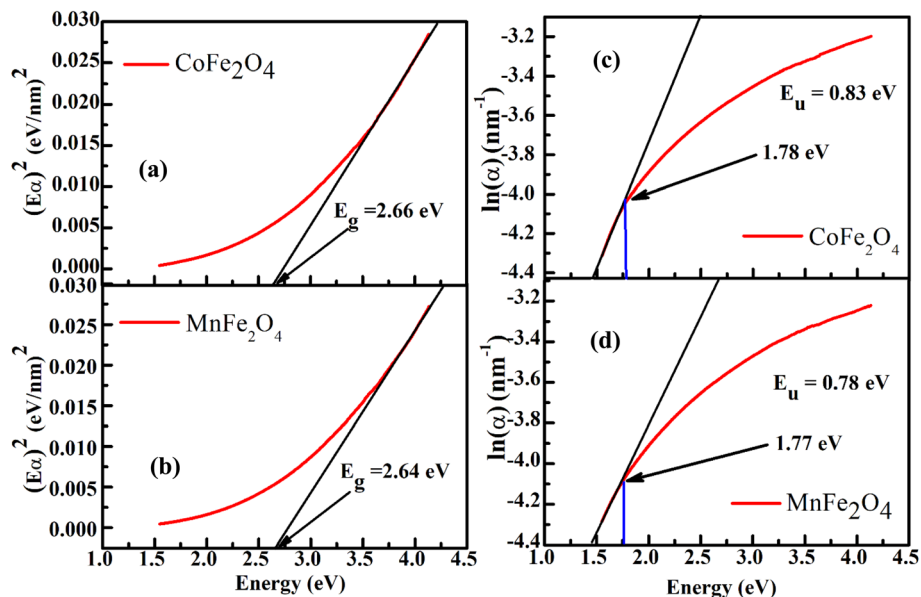


Fig. 6 (a and b) Tauc plots of  $\text{CoFe}_2\text{O}_4$  (a) and  $\text{MnFe}_2\text{O}_4$  (b) nanoparticles, showing  $(\alpha h\nu)^2$  as a function of photon energy ( $h\nu$ ). The red curves represent the experimental UV-vis absorption data, while the black lines indicate the linear fits used to estimate the optical bandgap by extrapolating to the photon energy axis. (c and d) Urbach plots for  $\text{CoFe}_2\text{O}_4$  (c) and  $\text{MnFe}_2\text{O}_4$  (d), where  $\ln(\alpha)$  is plotted versus photon energy ( $E$ ). The red curves correspond to the experimental data, and the black lines are linear fits to the Urbach region, from which the Urbach energy and optical absorption edge ( $E_0$ ) are determined.

energy absorption tail, were found to be 0.83 eV for  $\text{CoFe}_2\text{O}_4$  and 0.78 eV for  $\text{MnFe}_2\text{O}_4$ . Although the  $\text{MnFe}_2\text{O}_4$  sample exhibited a larger grain size, its  $E_u$  value was slightly lower than that of  $\text{CoFe}_2\text{O}_4$ . This observation suggests that the disorder in these spinel ferrites is not dominated solely by grain boundary density but also significantly influenced by oxygen vacancies, surface disorder, and cationic redistribution at the tetrahedral and octahedral sites.

To further explore the origin of this optical disorder, we examined its correlation with microstructural strain. The lattice strain, estimated *via* the Williamson–Hall method, increased markedly from  $0.52 \times 10^{-3}$  in  $\text{CoFe}_2\text{O}_4$  to  $2.48 \times 10^{-3}$  in  $\text{MnFe}_2\text{O}_4$ . Despite this significant rise in strain, the corresponding decrease in  $E_u$  implies that lattice strain alone does not dominate the density of localized states in the band tail. This inverse trend reinforces the view that  $E_u$  is not governed solely by macroscopic strain but rather by a combination of structural imperfections—including cation disorder and local bonding distortions—that are not fully captured by average strain measurements. These moderate  $E_u$  values in both systems reflect a notable degree of structural disorder, consistent with previous reports on spinel ferrites.<sup>68–71</sup>

Photoluminescence (PL) spectroscopy is a sensitive and non-destructive technique for investigating electron–hole recombination dynamics and evaluating the influence of surface and structural defects on the energy-band structure of ferrite nanomaterials.<sup>72</sup> In nanoscale systems, the high surface-to-volume ratio results in a large density of defect states—such as oxygen vacancies, surface dangling bonds, and cationic disorder—that serve as recombination centers. These defect states can significantly broaden the PL emission peaks and

reduce the overall intensity due to enhanced non-radiative recombination pathways, where excited carriers relax *via* thermal dissipation rather than photon emission.<sup>69</sup>

Fig. 7 illustrates the room-temperature PL spectra of  $\text{CoFe}_2\text{O}_4$  and  $\text{MnFe}_2\text{O}_4$  NPs in the 400–900 nm wavelength range. Both samples exhibited emission bands centered at approximately 458, 692, 753/758, and 871/882 nm, indicating multiple defect-related recombination pathways.

The PL spectra of both samples exhibit multiple emission bands arising from defect-related recombination pathways. The broad red emission band centered around 692 nm, observed in both  $\text{CoFe}_2\text{O}_4$  and  $\text{MnFe}_2\text{O}_4$ , along with near-infrared peaks at  $\sim 871$  nm and  $\sim 882$  nm, respectively, can be attributed to electron transitions from deep-level defect states—such as oxygen vacancies or antisite defects—to the valence band. The higher-wavelength emission in  $\text{MnFe}_2\text{O}_4$  is likely related to its narrower bandgap and greater degree of lattice disorder, which aligns with its larger Urbach energy. Additionally, the blue emission at  $\sim 458$  nm and the red band near 753/758 nm are assigned to transitions involving shallow trap states and surface defects, in agreement with the typical PL behavior reported for spinel ferrites. These peak assignments are consistent with previous reports on  $\text{CoFe}_2\text{O}_4$  and  $\text{MnFe}_2\text{O}_4$  nanoparticles,<sup>8,13,16,17,25,68,69</sup> which associate the observed PL emissions with intrinsic defects, such as oxygen vacancies,  $\text{Fe}^{2+}/\text{Fe}^{3+}$  transitions, and antisite disorder in the spinel lattice. While the PL intensity is generally expected to decrease with increasing defect density due to enhanced non-radiative recombination, some studies—such as that by Tongay *et al.*<sup>73</sup> on  $\text{MoS}_2$ ,  $\text{MoSe}_2$ , and  $\text{WSe}_2$ —have reported the opposite trend. This highlights the complex interplay between radiative and non-radiative



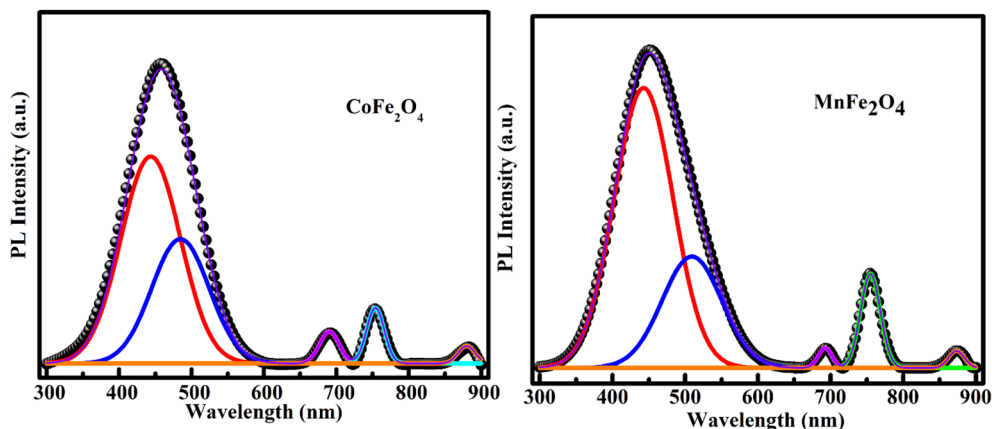


Fig. 7 Deconvolution of the photoluminescence (PL) spectra of  $\text{CoFe}_2\text{O}_4$  and  $\text{MnFe}_2\text{O}_4$  nanoparticles excited at 310 nm. The broad emission peak centred at 458 nm in both samples is resolved into two Gaussian components. In  $\text{CoFe}_2\text{O}_4$ , peaks at 443 nm (2.80 eV) and 485 nm (2.56 eV) are identified, while in  $\text{MnFe}_2\text{O}_4$ , the components appear at 443 nm (2.80 eV) and 509 nm (2.44 eV).

pathways in nanomaterials and reinforces the importance of interpreting PL results in conjunction with structural and optical analyses.

Therefore, to draw meaningful interpretations regarding electronic transitions and defect states in  $\text{MFe}_2\text{O}_4$  ( $\text{M} = \text{Co}, \text{Mn}$ ) NPs, the PL spectra must be considered in the broader context of the band structures of samples, which are derived from both UV-vis, PL and Urbach analyses.

The interpretation of the energy band structure and crystal field splitting energies ( $\Delta_{\text{cf},\text{O}}$  and  $\Delta_{\text{tf},\text{O}}$ ) in spinel ferrites containing 3d transition metal ions (e.g.,  $\text{Fe}^{3+}$ ,  $\text{Co}^{2+}$ ) remains a complex issue due to variability in synthesis methods and measurement techniques.<sup>74</sup> Consequently, reported values of crystal field splitting energies often show discrepancies across studies. For instance, Fontijn *et al.*<sup>75</sup> determined the octahedral crystal field splitting energy ( $\Delta_{\text{cf},\text{O}}$ ) for  $\text{Fe}^{3+}$  ions to be approximately 1.3 eV and the tetrahedral splitting energy ( $\Delta_{\text{tf},\text{O}}$ ) to be around 0.8 eV. Camphausen *et al.*<sup>76</sup> reported  $\Delta_{\text{cf},\text{O}}$  values between 1.7–2.0 eV and  $\Delta_{\text{tf},\text{O}}$  values from 0.86 to 1.17 eV. Boxall *et al.*<sup>77</sup> through photoelectrophoretic measurements, found  $\Delta_{\text{cf},\text{O}} = 2.2$  eV and  $\Delta_{\text{tf},\text{O}} = 0.8$  eV. In contrast, Alvarado *et al.*,<sup>78</sup> using spin polarization and energy distribution techniques, obtained  $\Delta_{\text{cf},\text{O}} = 1.75$  eV and  $\Delta_{\text{tf},\text{O}} = 1.55$  eV. For  $\text{Co}^{2+}$  ions, Fantechi *et al.*<sup>79</sup> reported  $\Delta_{\text{cf},\text{O}} = 1.22$  eV and  $\Delta_{\text{tf},\text{O}} = 1.77$  eV via Kerr photo-magnetic spectroscopy, while Papalardo *et al.*<sup>80</sup> and Kim *et al.*<sup>74</sup> found  $\Delta_{\text{tf},\text{O}}$  values of 0.83 eV and 2.2 eV, respectively. Overall, the literature suggests that  $\Delta_{\text{cf},\text{O}}$  for 3d ions generally lies in the range of 1.2–2.2 eV, whereas  $\Delta_{\text{tf},\text{O}}$  typically falls between 0.8 and 2.2 eV.<sup>74</sup>

Based on these findings and the results obtained in this work from UV-vis absorption, PL spectroscopy, and Urbach energy analyses, a comprehensive electronic band structure diagram was proposed for  $\text{MFe}_2\text{O}_4$  ( $\text{M} = \text{Co}, \text{Mn}$ ) nanoparticles (Fig. 8). The energy gap between the O(2p) valence band and the M(4s) conduction band is typically in the range of 4–6 eV for spinel ferrites.<sup>76,81,82</sup> Within this range, the 3d orbitals of transition metal ions split into distinct energy levels under crystal field interactions: for octahedral (B) sites, the splitting between  $t_{2g}$

and  $e_g$  levels is defined by  $\Delta_{\text{cf},\text{O}} \approx 1.75$  eV, and for tetrahedral (A) sites, the splitting between  $e$  and  $t_2$  levels is characterized by  $\Delta_{\text{tf},\text{O}} \approx 0.8$  eV.<sup>74</sup> Additional splitting ( $\sim 0.9$  eV) between the O(2p) valence band and the  $t_{2g}/e$  levels further modulates the band structure, as observed in various experimental reports.<sup>75,77</sup> The bandgap energy extracted from Tauc plots (Fig. 6(a and b)) was 2.66 eV for  $\text{CoFe}_2\text{O}_4$  and 2.64 eV for  $\text{MnFe}_2\text{O}_4$ , corresponding well to the transition from the O(2p) level to the  $e_g$  level in the B crystal field. Moreover, the onset of absorption observed in the Urbach plots (Fig. 6c and d) appears to correspond closely with  $\Delta_{\text{cf},\text{O}}$  ( $\sim 1.75$  eV) or transitions from the O(2p) band to the  $t_2$  level of the A field ( $\sim 1.8$  eV). These values support the involvement of localized sub-bandgap states in the optical absorption process.

The presence of oxygen vacancies and lattice distortions, as previously evidenced by Williamson–Hall analysis and FTIR spectral features, suggests the existence of localised defect

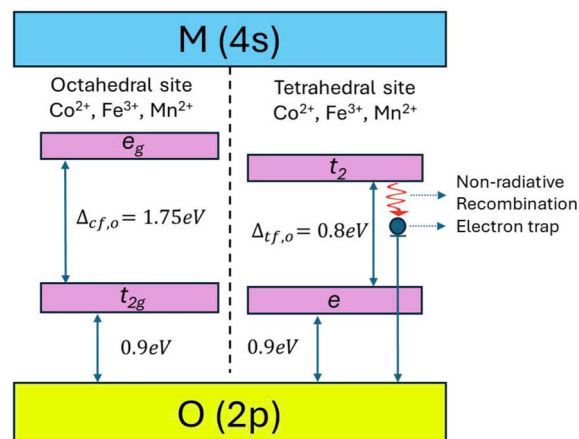


Fig. 8 Schematic of the proposed energy band structure for  $\text{MFe}_2\text{O}_4$  ( $\text{M} = \text{Co}, \text{Mn}$ ) nanoparticles. The diagram is constructed based on UV-vis absorption, PL spectra, and Urbach tail analysis. This diagram elucidates the correlation among crystal field environments, cation distribution, and optical transitions in spinel ferrites.



states within the bandgap of both  $\text{CoFe}_2\text{O}_4$  and  $\text{MnFe}_2\text{O}_4$ . These structural imperfections are expected to play a significant role in charge carrier dynamics. Under excitation at 310 nm ( $\sim 4.0$  eV), electrons are promoted to high-energy states such as the  $e_g$  orbital at the B-site cations, followed by radiative or non-radiative relaxation. Initially, both samples exhibited a broad PL emission peak centred at 458 nm (2.70 eV), which coincides with the optical bandgap obtained from UV-vis absorption, suggesting a possible direct transition from the conduction band to the O(2p) valence band.

However, Gaussian deconvolution of the PL spectra revealed that this apparent single peak comprises two components: 443 nm (2.80 eV) and 485 nm (2.56 eV) in  $\text{CoFe}_2\text{O}_4$ , and 443 nm (2.80 eV) and 509 nm (2.44 eV) in  $\text{MnFe}_2\text{O}_4$ . The higher-energy emission at 2.80 eV may be attributed to excitonic transitions or recombination *via* shallow donor states, while the lower-energy bands are ascribed to deep-level defect emissions, possibly involving oxygen vacancies or  $\text{Fe}^{3+}/\text{Co}^{2+}$  trap states. These observations indicate that, although near-band-edge transitions are present, defect-assisted recombination processes dominate the photoluminescence behaviour of both ferrite systems. The red emission at 692 nm (1.79 eV) can be attributed either to  $t_{2g} \rightarrow e_g$  transitions in the B site or to electron recombination from the e orbital in the A site to the O(2p) valence band. The weaker red emission at 753 nm (1.65 eV) likely originates from  $e \rightarrow t_2$  transitions within the A site. Lastly, the near-infrared emissions at 871 nm (1.42 eV) for  $\text{CoFe}_2\text{O}_4$  and 882 nm (1.40 eV) for  $\text{MnFe}_2\text{O}_4$  are attributed to deep trap states associated with oxygen vacancies and cation disorder in the A site lattice environment. These energy transitions are coherent with the proposed schematic (Fig. 8), demonstrating the strong correlation between electronic structure, defect states, and the optical behavior of spinel ferrite nanoparticles.

The combined structural and spectroscopic analyses of  $\text{CoFe}_2\text{O}_4$  and  $\text{MnFe}_2\text{O}_4$  nanoparticles reveal a coherent picture of how cation distribution, crystallite size, and surface defect states modulate their optical and electronic properties. The constructed energy band schematic captures the essential transitions involving the O(2p)  $\rightarrow$  3d crystal field levels, explaining both the band-edge absorption and PL emission behaviors. Notably, blue and red emissions were matched with recombinations involving  $e_g \rightarrow \text{O}(2p)$  and  $t_{2g} \rightarrow e_g$  transitions, while near-infrared emissions were attributed to electron traps associated with oxygen vacancies. Together, these findings underscore the importance of controlled cation distribution and structural order in tailoring the optical and electronic performance of spinel ferrite nanoparticles for applications in magneto-optical, photocatalytic, and biomedical technologies.

The proposed energy band diagrams for  $\text{MnFe}_2\text{O}_4$  nanoparticles were constructed based on the experimental UV-vis absorption and PL data. The band edge positions and defect-related emission features were interpreted in conjunction with literature reports on similar spinel ferrites,<sup>69,75,77</sup> facilitating a qualitative but coherent description of electronic transitions and energy transfer mechanisms. Although direct probing of the electronic structure through techniques such as

X-ray photoelectron spectroscopy (XPS), ultraviolet photoelectron spectroscopy (UPS), or density functional theory (DFT) calculations was not performed, theoretical data from previous studies were incorporated to enhance the credibility of the proposed models.

For  $\text{CoFe}_2\text{O}_4$ , the direct optical band gap obtained from the UV-vis spectra (2.66 eV) was found to be consistent with previous experimental reports ( $\sim 2.7$  eV), and lies within the range of DFT-calculated values (1.0–2.3 eV), depending on the functional employed.<sup>83</sup> This transition has generally been attributed to the O(2p)  $\rightarrow$  Co(3d) charge transfer at the band edges.<sup>83</sup>

In the case of  $\text{MnFe}_2\text{O}_4$ , a direct band gap of 2.64 eV was determined, which agrees with prior optical measurements on nanoscale  $\text{MnFe}_2\text{O}_4$  ( $\sim 2.6$  eV).<sup>84</sup> In contrast, standard DFT approaches have been shown to underestimate the band gap, yielding values as low as 0.4 eV.<sup>85</sup> More accurate GGA + U calculations have been reported to yield values around 1.3 eV,<sup>86</sup> and other studies have suggested values ranging from 1.3 to 1.6 eV depending on the degree of cation ordering and particle size.<sup>84,87</sup> The larger experimental band gap observed in this study may be attributed to quantum confinement and surface effects, which have been well documented in spinel ferrites.<sup>88,89</sup>

Overall, the experimentally determined band gaps were found to align well with both theoretical predictions and previously published results. The PL emission bands, which were associated with deep-level defect states, were observed to correlate with features in the calculated density of states reported in the literature. Accordingly, even in the absence of direct DFT computations, the proposed energy band diagrams are supported by a consistent and converging body of prior theoretical and experimental evidence.

Mie theory offers a robust framework for quantitatively assessing the photothermal performance of nanomaterials by analyzing their light–matter interactions. Specifically, the wavelength dependence of three key optical parameters—absorption efficiency ( $Q_{\text{abs}}$ ), extinction efficiency ( $Q_{\text{ext}}$ ), and scattering efficiency ( $Q_{\text{sca}}$ )—was investigated for the  $\text{CoFe}_2\text{O}_4$  and  $\text{MnFe}_2\text{O}_4$  NPs. These parameters are defined by the following equations:<sup>69,81</sup>

$$Q_{\text{ext}} = \frac{2}{x^2} \sum_{n=1}^{\infty} (2n+1) \text{Re}[a_n + b_n], \quad (4a)$$

$$Q_{\text{sca}} = \frac{2}{x^2} \sum_{n=1}^{\infty} (2n+1) \left[ |a_n|^2 + |b_n|^2 \right], \quad (4b)$$

$$Q_{\text{abs}} = Q_{\text{ext}} - Q_{\text{sca}}, \quad (4c)$$

Here,  $a_n$  and  $b_n$  are Mie scattering coefficients and  $x = \frac{2\pi n_{\text{med}} D}{\lambda_0}$  is the size parameter, where  $D$  is the particle radius,  $n_{\text{med}}$  is the refractive index of the surrounding medium, and  $\lambda_0$  is the vacuum wavelength of incident light.

Numerical computations of these parameters as functions of wavelength were carried out using the “MiePlot” simulation software developed by Philip Laven.<sup>90</sup> As shown in Fig. 9,



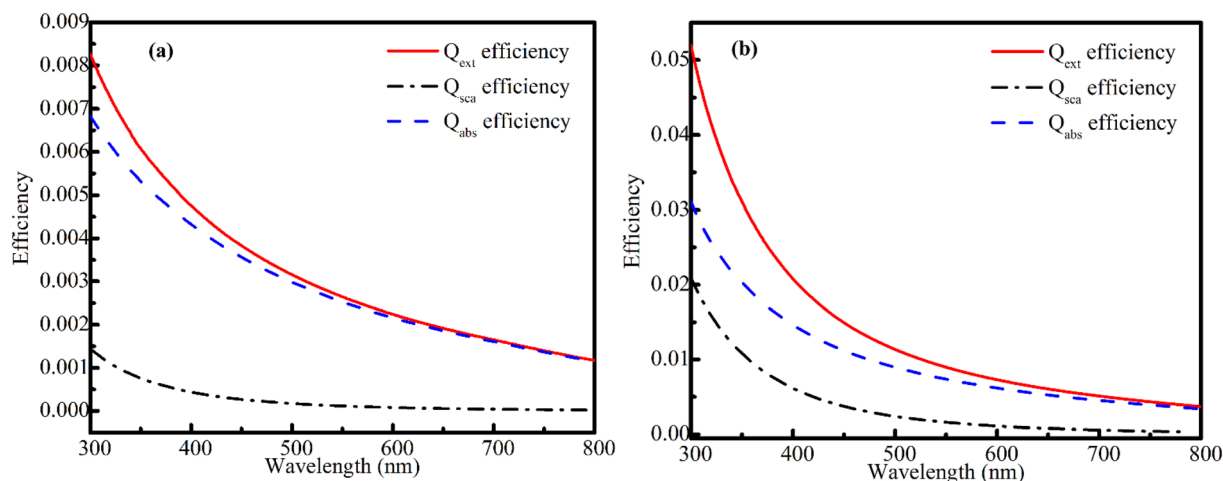


Fig. 9 The wavelength dependence of extinction ( $Q_{\text{ext}}$ ), absorption ( $Q_{\text{abs}}$ ), and scattering ( $Q_{\text{sca}}$ ) efficiencies for (a)  $\text{CoFe}_2\text{O}_4$  NPs and (b)  $\text{MnFe}_2\text{O}_4$  NPs. The parameters are determined from the Mie theory using eqn 4(a)–(c).

$\text{CoFe}_2\text{O}_4$  NPs exhibited a dominant absorption contribution to extinction efficiency in the longer wavelength region ( $>650$  nm), suggesting effective conversion of light into heat in this spectral range. In contrast,  $\text{MnFe}_2\text{O}_4$  NPs showed negligible absorption contribution across the entire studied wavelength range, implying low photothermal conversion efficiency.

The ratio of absorption to extinction efficiency ( $Q_{\text{abs}}/Q_{\text{ext}}$ )—a key indicator of photothermal conversion capability—was substantially higher for  $\text{CoFe}_2\text{O}_4$  than for  $\text{MnFe}_2\text{O}_4$ . In the context of Mie theory, the absorption efficiency ( $Q_{\text{abs}}$ ) quantifies the fraction of incident light that is absorbed by the nanoparticle and subsequently converted into other forms of energy, such as heat. Meanwhile, scattering efficiency ( $Q_{\text{sca}}$ ) represents the portion of light that is elastically scattered by the particle without absorption. The total extinction efficiency ( $Q_{\text{ext}}$ ) is the sum of these two contributions, reflecting the overall interaction of light with the particle. A higher  $Q_{\text{abs}}/Q_{\text{ext}}$  ratio indicates that a greater fraction of the light interacting with the particle is being absorbed rather than scattered, which is a desirable feature for efficient photothermal conversion. This observation aligns with the smaller particle size and higher specific surface area of  $\text{CoFe}_2\text{O}_4$ , both of which are known to enhance light absorption and heat generation.<sup>69</sup> Additionally, the scattering efficiency was significantly higher for  $\text{MnFe}_2\text{O}_4$ , which can be attributed to its larger particle size and is consistent with classical Mie scattering predictions. While the current analysis relies on Mie theory to estimate photothermal behavior, it offers valuable insight into the interplay between nanoparticle size, composition, and optical response. We acknowledge that the absence of direct experimental photothermal measurements is a limitation of the present work. Nevertheless, theoretical modeling serves as a predictive tool for evaluating wavelength- and size-dependent photothermal efficiency. Future studies will aim to experimentally validate these findings and benchmark the photothermal performance of  $\text{CoFe}_2\text{O}_4$  and  $\text{MnFe}_2\text{O}_4$  nanoparticles against established photothermal agents such as gold, silver, or copper sulfide nanostructures.

### 3.4. Magnetic properties of $\text{MnFe}_2\text{O}_4$ NPs

Fig. 10 presents the room-temperature magnetic hysteresis loops ( $M$ - $H$  curves) of  $\text{CoFe}_2\text{O}_4$  and  $\text{MnFe}_2\text{O}_4$  NPs, illustrating their distinct magnetic behavior. Key magnetic parameters, including remanent magnetization ( $M_r$ ) and coercivity ( $H_c$ ), were extracted directly from the loops and are summarized in Table 3. To obtain a more accurate estimation of the saturation magnetization ( $M_s$ ) and magnetocrystalline anisotropy constant ( $K_1$ ), the initial magnetization curves were fitted using the Law of Approach to Saturation (LAS), which accounts for high-field magnetization behavior and spin deviation near saturation. The LAS equation is expressed as:<sup>91,92</sup>

$$M(H) = M_s \left( 1 - \frac{a}{H} - \frac{b}{H^2} \right) + \chi_d H, \quad (5)$$

where  $\chi_d$  is the forced-magnetization coefficient, whose contribution is dominant at temperatures above the Curie temperature, and the term  $a/H$  represents the inhomogeneity of the material, whose contribution can be ignored at high magnetic fields. In particular, the second-order term  $b/H^2$  dominates in high-field regions and is directly related to the effective magnetic anisotropy constant ( $K_1$ ) according to the following equation:

$$b = \frac{8K_1^2}{105M_s^2}. \quad (6)$$

The fitting of magnetization  $M(H)$  data to the Law of Approach to Saturation (LAS) model reached convergence only when the sum of squared residuals (SSR) was minimized. This condition was satisfied by selectively adjusting the parameters  $b$  and  $M_s$  within the high-field region ( $H > 1.0$  T), where the approach to magnetic saturation becomes more pronounced. Fig. 11 displays both the experimental  $M(H)$  curves and the theoretical fits derived from the LAS model for  $\text{CoFe}_2\text{O}_4$  and  $\text{MnFe}_2\text{O}_4$  samples. The optimized values of the fitting



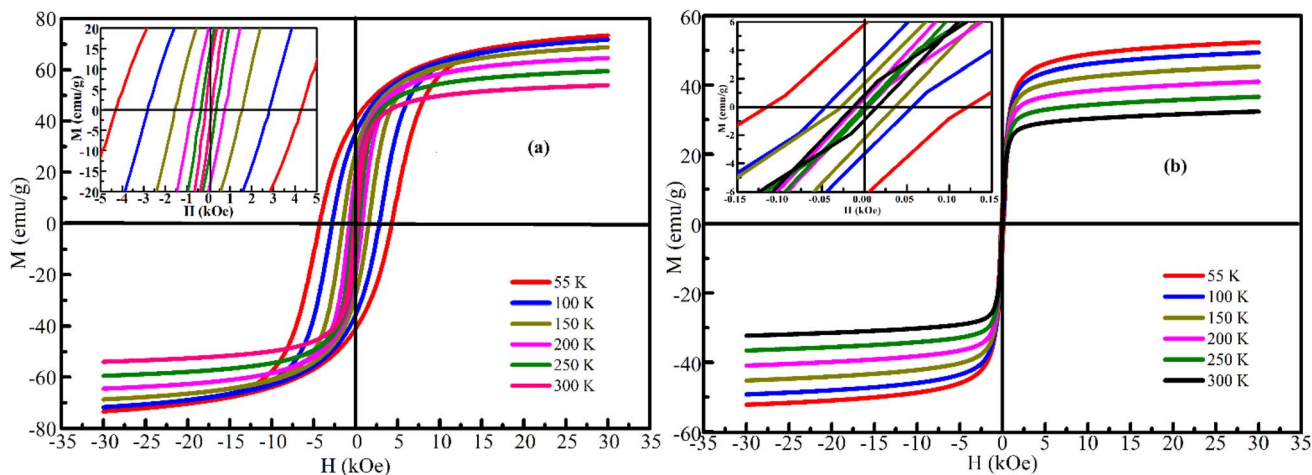


Fig. 10 The typical hysteresis loop of  $\text{CoFe}_2\text{O}_4$  NPs (a) and  $\text{MnFe}_2\text{O}_4$  NPs (b) for different temperatures. The insets are an enlargement of the magnetization at low field.

parameters  $b$  and  $M_s$  at different temperatures are summarized in Table 3.

Using eqn (6), the magnetocrystalline anisotropy constant  $K_1$  was calculated by substituting the obtained values of  $b$  and  $M_s$ . The resulting  $K_1$  values, corresponding to the range of studied temperatures, are also listed in Table 3. Notably, at all temperatures, the  $K_1$  value for  $\text{CoFe}_2\text{O}_4$  was significantly higher than that for  $\text{MnFe}_2\text{O}_4$ , consistent with the known strong anisotropy of cobalt ferrites. Furthermore, the variation of  $K_1$  with temperature for both samples followed the expected trends, reflecting the thermal dependence of magnetic anisotropy in spinel ferrites. These findings confirm the strong dependence of magnetic anisotropy on the type of transition metal cation occupying the octahedral (B) site in the spinel structure. The higher  $K_1$  values observed for  $\text{CoFe}_2\text{O}_4$  across all temperatures reflect the dominant contribution of  $\text{Co}^{2+}$  ions, which exhibit significant spin-orbit coupling and strong magnetocrystalline anisotropy. In contrast, the relatively lower  $K_1$  values for  $\text{MnFe}_2\text{O}_4$  are attributed to the weaker anisotropy of  $\text{Mn}^{2+}$  ions in similar coordination environments. Additionally,

the saturation magnetization  $M_s$  of  $\text{CoFe}_2\text{O}_4$  was consistently higher than that of  $\text{MnFe}_2\text{O}_4$ , which can be explained by differences in cation distribution and magnetic interactions between the A- and B-site ions. The partially inverse spinel structure of  $\text{CoFe}_2\text{O}_4$  likely facilitates enhanced superexchange interactions between  $\text{Fe}^{3+}$  ions at the tetrahedral (A) and octahedral (B) sites, thereby increasing  $M_s$ . Meanwhile,  $\text{MnFe}_2\text{O}_4$  exhibits lower  $M_s$ , possibly due to spin canting or surface disorder effects that are more pronounced in cobalt-based ferrites. The temperature dependence of  $K_1$  for both  $\text{CoFe}_2\text{O}_4$  and  $\text{MnFe}_2\text{O}_4$  was consistent with previously reported values in the literature.<sup>93–95</sup> The observed increase in  $K_1$  can be attributed to a combination of (i) surface anisotropy, (ii) dipolar interactions, and (iii) the nanocrystalline nature of the particles with small grain sizes.<sup>96</sup> Furthermore, both samples exhibited similar magnetic trends with temperature: saturation magnetization and coercivity increased as the temperature decreased. The monotonic increase in  $M_s$  is primarily due to the enhancement of exchange interactions between neighboring magnetic moments at lower temperatures, consistent with the

Table 3 Saturation magnetization ( $M_s$ ), remnant magnetization ( $M_r$ ), coercivity ( $H_c$ ), second-order coefficient ( $b$ ), first-order cubic anisotropy constant ( $K_1$ ) and squareness ratio ( $M_r/M_s$ ) of  $\text{CoFe}_2\text{O}_4$  and  $\text{MnFe}_2\text{O}_4$  nanoparticles at various temperatures

Sample	Temp. (K)	$M_s$ ( $\text{emu g}^{-1}$ )	$M_s$ ( $\mu_B$ )	$M_r$ ( $\text{emu g}^{-1}$ )	$H_c$ (Oe)	$M_r/M_s$	$b \times 10^6$ ( $\text{Oe}^2$ )	$K_1 \times 10^6$ ( $\text{erg cm}^{-3}$ )
$\text{CoFe}_2\text{O}_4$	55	70.10	2.94	40.32	4333.43	0.58	17.42	5.53
	100	67.96	2.85	35.15	2809.84	0.52	12.92	4.62
	150	65.67	2.76	28.12	1972.03	0.43	10.79	4.08
	200	61.85	2.60	20.01	996.65	0.32	8.80	3.47
	250	57.05	2.40	12.5	522.20	0.22	7.27	2.91
	300	51.60	2.18	7.24	146.01	0.14	6.14	2.42
$\text{MnFe}_2\text{O}_4$	55	49.90	2.06	5.87	126.65	0.12	5.00	2.03
	100	46.86	1.93	2.73	51.95	0.06	4.79	1.87
	150	42.81	1.77	1.64	28.33	0.04	4.29	1.62
	200	38.57	1.59	0.636	11.84	0.02	3.92	1.39
	250	34.36	1.42	0.24	5.12	0.01	3.52	1.17
	300	30.25	1.25	0.85	15.10	0.03	3.18	0.98



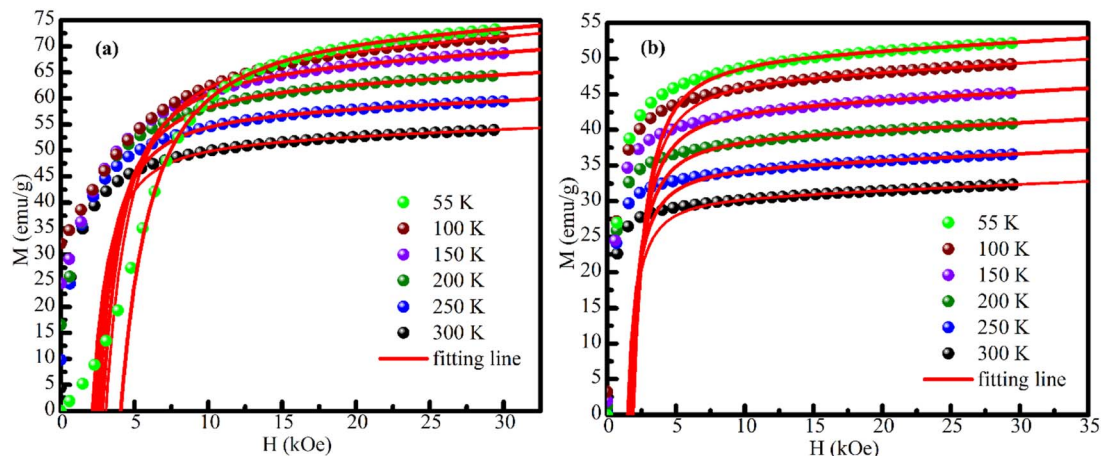


Fig. 11 Experimental and fitted magnetization curves of (a)  $\text{CoFe}_2\text{O}_4$  and (b)  $\text{MnFe}_2\text{O}_4$  nanoparticles at selected temperatures based on the law of approach to saturation (LAS). The solid dots represent experimental  $M$ - $H$  data, and the solid lines denote the best-fit curves obtained by minimizing the sum of squared residuals.

suppression of spin-wave excitations. This behavior follows Bloch's  $T^{3/2}$  law<sup>92,97</sup>

$$M_s(T) = M_s(0)(1 - AT^{3/2}), \quad (7)$$

where  $M_s(T)$  is the saturation magnetization at temperature  $T$ ,  $M_s(0)$  is the extrapolated value at 0 K, and  $A$  is the Bloch's constant. As shown in Fig. 12, the experimental  $M_s(T)$  data of both samples fit well with this model. The inset of Fig. 12 further confirms this by plotting  $[(M_s(0) - M_s(T))/M_s(0)]$  as a function of temperature ( $T$ ). The extracted Bloch constants were  $A \approx 5.34 \times 10^{-5} \text{ K}^{-3/2}$  for  $\text{CoFe}_2\text{O}_4$  and  $A \approx 8.07 \times 10^{-5} \text{ K}^{-3/2}$  for  $\text{MnFe}_2\text{O}_4$ , in agreement with the values reported for other spinel ferrites,<sup>98</sup> reflecting their structural similarities. The extrapolated  $M_s(0)$  values were  $72.14 \text{ emu g}^{-1}$  (equivalent to  $3.03 \mu_B$ ) for  $\text{CoFe}_2\text{O}_4$  and  $50.87 \text{ emu g}^{-1}$  ( $2.10 \mu_B$ ) for  $\text{MnFe}_2\text{O}_4$ . These experimental results were slightly lower than the

theoretical magnetic moments estimated from cation distributions (Table 1), which yielded  $\sim 5.64 \mu_B$  for  $\text{CoFe}_2\text{O}_4$  ( $3 \mu_B \times 0.34 + 5 \mu_B \times 1.66 - 3 \mu_B \times 0.66 - 5 \mu_B \times 0.34$ ) and  $\sim 5.00 \mu_B$  ( $5 \mu_B \times 0.33 + 5 \mu_B \times 1.67 - 5 \mu_B \times 0.67 - 5 \mu_B \times 0.33$ ) for  $\text{MnFe}_2\text{O}_4$ , where the ionic magnetic moments of  $\text{Fe}^{3+}$ ,  $\text{Co}^{2+}$  and  $\text{Mn}^{2+}$  were  $5$ ,  $3$ , and  $5 \mu_B$ , respectively. The experimentally determined  $M_s(0)$  values for both samples were lower than the theoretical predictions, likely due to a reduction in the A-B superexchange interactions as described by the three-sublattice Yafet-Kittel model,<sup>99</sup> along with the influence of the surface spin disorder inherently associated with nanoparticle systems.

To investigate the role of surface anisotropy, dipolar interactions, and nanocrystalline grain effects on the magnetic behavior of  $\text{CoFe}_2\text{O}_4$  and  $\text{MnFe}_2\text{O}_4$  nanoparticles, the squareness ratio ( $R = M_r/M_s$ ) was determined at various temperatures and is summarized in Table 3. According to the Stoner-

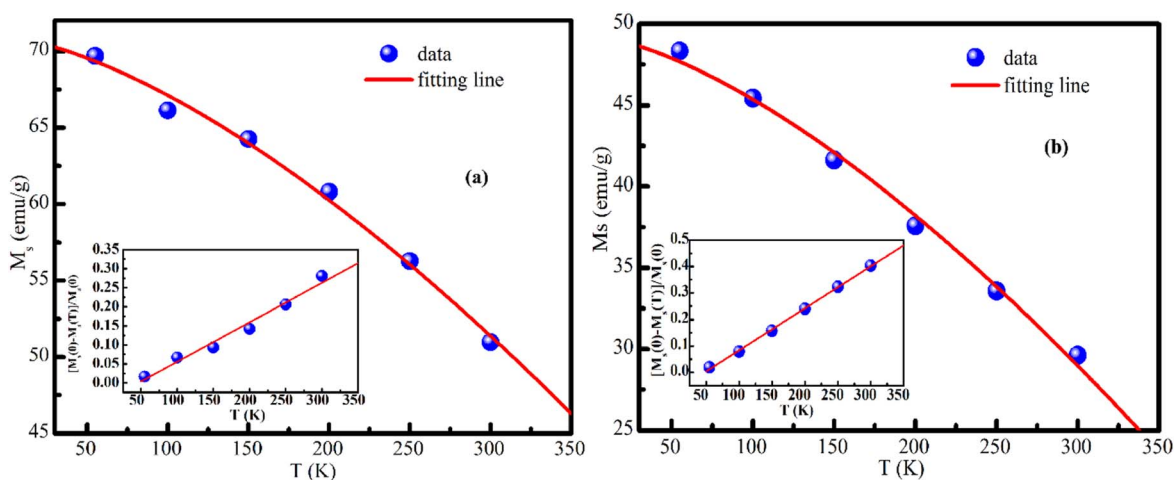


Fig. 12 Temperature dependence of the saturation magnetization for (a)  $\text{CoFe}_2\text{O}_4$  and (b)  $\text{MnFe}_2\text{O}_4$  nanoparticles. The solid red lines indicate the fitting to Bloch's law, as described in the text. Insets show the reduced magnetization,  $[M_s(0) - M_s(T)]/M_s(0)$ , plotted as a function of temperature to highlight the spin-wave excitation behavior.



Wohlfarth (SW) model, which assumes an ensemble of randomly oriented, non-interacting, single-domain particles, the ideal squareness ratio is  $R = 0.5$ . For uniaxially aligned particles without thermal agitation, the model predicts a higher ratio of  $R = 0.832$ . It is important to note that both values neglect thermal fluctuation effects. As shown in Table 3, the  $\text{CoFe}_2\text{O}_4$  sample exhibits an  $R$  value of approximately 0.6 at 55 K, which decreases to 0.14 at 300 K. This trend suggests that the  $\text{CoFe}_2\text{O}_4$  nanoparticles possess cubic magnetocrystalline anisotropy at low temperatures, consistent with previous reports on monodisperse  $\text{CoFe}_2\text{O}_4$  NPs,<sup>100</sup> single-domain  $\text{CoFe}_2\text{O}_4$  systems,<sup>101</sup> and  $\text{CoFe}_2\text{O}_4/\text{CTAB}$  nanocomposites.<sup>102</sup> In contrast, the  $\text{MnFe}_2\text{O}_4$  sample exhibits a very low squareness ratio ( $R < 0.1$ ) across all temperatures studied. The low squareness ratio observed in  $\text{MnFe}_2\text{O}_4$  can be attributed to several factors, including its relatively larger average particle size, broader size distribution, and possible surface spin disorder. These structural characteristics are known to enhance magnetostatic (dipolar) interactions and magnetic relaxation phenomena, which collectively suppress remanent magnetization. The notably small squareness value also suggests the presence of strong interparticle magnetic interactions, thereby violating the assumptions of the Stoner–Wohlfarth model, which is valid only for non-interacting, single-domain particles with uniaxial anisotropy.<sup>103</sup> This behavior is consistent with the soft magnetic nature and possible superspin glass (SSG) tendencies observed in the  $\text{MnFe}_2\text{O}_4$  sample. For both samples, the observed  $R$  values are lower than the theoretical limit of 0.5, which is frequently observed in magnetic nanostructures and generally attributed to surface spin disorder and frustration effects. Consequently, while the SW model can still provide qualitative insights into the behavior of  $\text{CoFe}_2\text{O}_4$ , it appears unsuitable for describing the  $\text{MnFe}_2\text{O}_4$  system. The relatively high squareness ratio (up to 0.6 at 55 K) for  $\text{CoFe}_2\text{O}_4$  further supports the presence of significant surface anisotropy, influencing its magnetocrystalline anisotropy constant  $K_1$ . This is consistent with the known high cubic anisotropy of  $\text{CoFe}_2\text{O}_4$ , which has a theoretical  $R \approx 0.832$  and  $K_1 > 0$ . The maximum value of  $K_1$  observed in this study was  $5.37 \times 10^6$  erg  $\text{cm}^{-3}$  at 55 K—substantially higher than that reported for bulk  $\text{CoFe}_2\text{O}_4$  (typically in the range of  $1.8$ – $3.0 \times 10^6$  erg  $\text{cm}^{-3}$ ).<sup>104</sup> Such enhanced values can be attributed to increased surface contributions, reduced grain size, and strong dipolar interactions.

Conversely, lower  $K_1$  values are generally indicative of weaker intrinsic anisotropy and enhanced thermal agitation at higher temperatures.

Additional evidence for the presence of magnetic interactions in both nanoparticle systems can be derived from their temperature-dependent coercivity behavior. According to Kneller's law,<sup>105</sup> the coercive field  $H_c(T)$  follows a square-root temperature dependence in single-domain systems:

$$H_c(T) = H_c(0)[1 - (T/T_B)^{1/2}], \quad (8)$$

where  $H_c(0)$  is the coercive field at absolute zero, and  $T_B$  is the blocking temperature. The validity of this expression can provide further insight into the magnetic relaxation and interaction mechanisms in the samples. As shown in Fig. 13, the coercivity data of  $\text{CoFe}_2\text{O}_4$  nanoparticles exhibit a good fit to Kneller's law in the temperature range of  $55\text{K} \leq T < 300\text{K}$ . This agreement suggests that the  $\text{CoFe}_2\text{O}_4$  NPs behave as monodisperse, non-interacting, single-domain particles with ferromagnetic ordering.<sup>106</sup> The fitting yielded values of  $H_c(0) = 7542$  Oe and  $T_B = 276$  K, confirming the validity of the single-domain model for this system. In contrast, the coercivity of  $\text{MnFe}_2\text{O}_4$  nanoparticles did not conform to Kneller's law over the studied temperature range, indicating the presence of significant magnetic interactions, particle size distribution, or a multi-domain nature in the  $\text{MnFe}_2\text{O}_4$  system.

To gain further insight into the magnetic transition behavior and confirm the thermal stability of the nanoparticles, temperature-dependent magnetization measurements were conducted in the range of 55–350 K. Fig. 14 shows the temperature-dependent magnetization curves measured under zero-field-cooled (ZFC) and field-cooled (FC) conditions and an applied field of 10 Oe for the  $\text{CoFe}_2\text{O}_4$  and  $\text{MnFe}_2\text{O}_4$  samples, respectively. For  $\text{MnFe}_2\text{O}_4$ , both FC and ZFC curves exhibit a gradual decrease with decreasing temperature. The FC curve decreases slowly, while the ZFC curve shows a more pronounced drop at low temperatures, which is commonly associated with surface spin freezing. This behavior has been previously reported<sup>107</sup> and is often attributed to an SSG state, induced by strong interparticle dipolar interactions. Notably, the FC and ZFC curves nearly converge above 325 K, suggesting the onset of reversible superparamagnetic behavior beyond the blocking temperature ( $T_B$ ), which is not reached within the measured

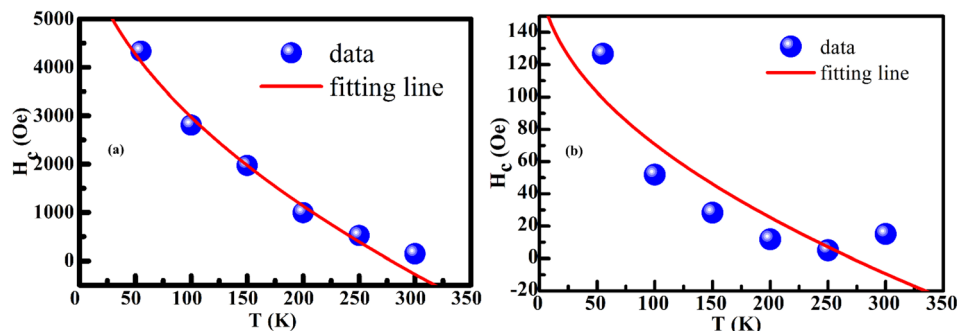


Fig. 13 Fitting to the Kneller's law for  $\text{CoFe}_2\text{O}_4$  NPs (a) and  $\text{MnFe}_2\text{O}_4$  NPs (b).

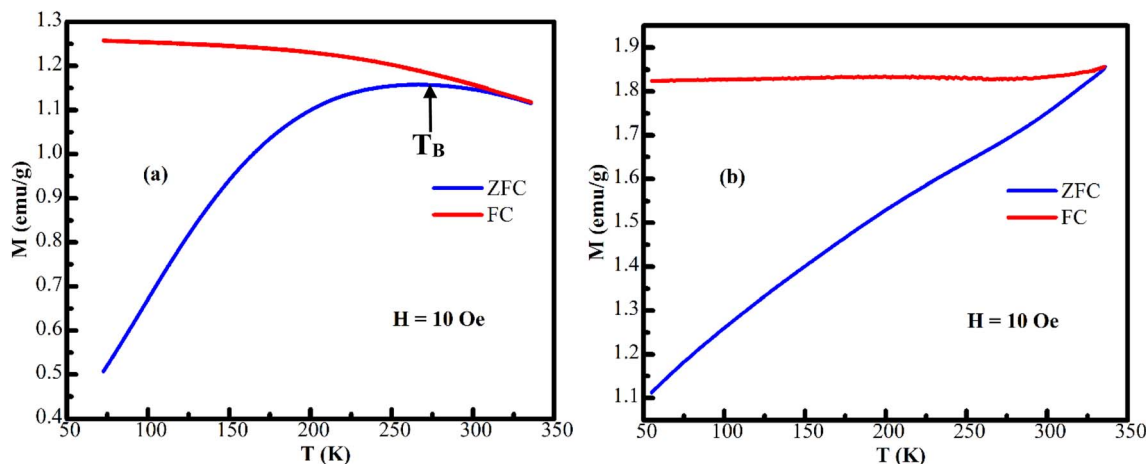


Fig. 14 ZFC and FC magnetization curves of (a)  $\text{CoFe}_2\text{O}_4$  and (b)  $\text{MnFe}_2\text{O}_4$  measured at 10 Oe in the temperature range of 55–350 K. The blocking temperature ( $T_B$ ) for  $\text{CoFe}_2\text{O}_4$  is indicated by a dashed vertical line. For  $\text{MnFe}_2\text{O}_4$ ,  $T_B$  lies above the measurement range, as suggested by the convergence of FC/ZFC curves at high temperatures.

range ( $T_B > 350$  K). This trend is consistent with the very low coercivity observed at room temperature ( $H_c \sim 15$  Oe at 300 K). In contrast, the  $\text{CoFe}_2\text{O}_4$  sample exhibits clear separation between the ZFC and FC curves up to 310 K, with a distinct  $T_B$  observed near 276 K. Below this point, the FC magnetization increases steadily with decreasing temperature, while the ZFC curve exhibits a peak and then decreases due to magnetic relaxation. The larger separation between the FC and ZFC curves reflects stronger magnetic anisotropy and more stable blocked states. This correlates well with the higher coercivity of  $\text{CoFe}_2\text{O}_4$  ( $H_c \sim 522$  Oe at 250 K) and suggests minimal influence of dipolar interactions, as reported in similar systems, such as  $\text{Fe}_3\text{O}_4$  nanocrystals<sup>108</sup> and others.<sup>109</sup>

It is important to distinguish between superparamagnetic (SPM) and SSG behaviors, both of which can manifest in nanoparticle systems depending on size distribution and interparticle interactions. In the SPM regime, each nanoparticle behaves like a single magnetic domain whose net magnetic moment can thermally fluctuate and align with the external field above the blocking temperature ( $T_B$ ), leading to reversible FC and ZFC magnetization curves. In contrast, the SSG state arises from strong dipolar interactions among nanoparticles, which lead to frustrated collective spin freezing at low temperatures, analogous to atomic spin glasses. This behavior is typically characterized by a bifurcation between the FC and ZFC curves that does not converge even at high temperatures, broad peaks or the absence of peaks in the ZFC curves, and low coercivity at room temperature. In our study, the observed magnetic features of  $\text{MnFe}_2\text{O}_4$ —such as the slow decay of FC magnetization, suppressed ZFC peak, and high-temperature bifurcation—are consistent with the SSG-like behavior. Meanwhile,  $\text{CoFe}_2\text{O}_4$  exhibits typical SPM features with a clear  $T_B$  and larger coercivity due to stronger magnetic anisotropy.

The magnetic behavior of an ideal, non-interacting superparamagnetic system is characterized by the collapse of all  $M/M_s$  curves versus  $H/T$  curves onto a single universal curve. These

normalized magnetization curves should follow the classical Langevin function:

$$M = N\mu L\left(\frac{\mu H}{k_B T}\right), \quad (9a)$$

where  $\mu$  is the magnetic moment of a single particle,  $N$  is the number of particles per unit volume,  $k_B$  is the Boltzmann's constant, and  $L$  is the Langevin function. The saturation magnetization is given by  $M_s = N\mu$ .

However, in systems where dipolar interactions are present, deviations from this ideal behavior are often observed. To account for such interactions, Allia *et al.*<sup>110</sup> proposed a modified Langevin function that incorporates an effective interaction temperature  $T^*$ , which is related to the dipolar interaction energy  $\varepsilon_D$  by the expression:

$$\varepsilon_D = k_B T^*, \quad (9b)$$

The modified expression becomes:

$$M = N\mu L\left(\frac{\mu H}{k_B (T + T^*)}\right), \quad (9c)$$

For the  $\text{MnFe}_2\text{O}_4$  nanoparticles studied here, the experimental ( $M/M_s$ ) versus  $H/T$  curves shown in Fig. 15(a) deviate from the universal behavior predicted by the classical Langevin model, indicating the presence of interparticle magnetic interactions. However, when the data are replotted as a function of  $H/M_s$ , the curves collapse onto a single master curve that follows the modified Langevin behavior, as illustrated in Fig. 15(b). This observation supports the existence of an interacting superparamagnetic regime.

To provide a quantitative measure of dipolar interactions, the experimental magnetization curves were fitted using the modified Langevin model. The fitting yielded an effective interaction temperature of approximately  $T^* \approx 120$  K. From this value, the dipolar interaction energy was estimated as:  $\varepsilon_D = k_B T^*$



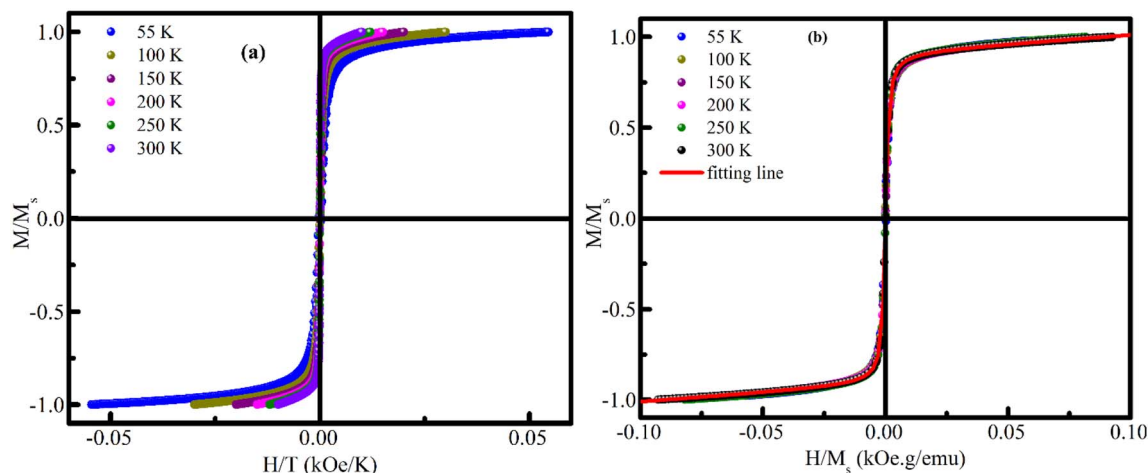


Fig. 15 Relative magnetization ( $M/M_s$ ) of  $\text{MnFe}_2\text{O}_4$  NPs measured at six different temperatures plotted as a function of  $(H/T)$  (a) and  $H/M_s$  (b), according to the interacting superparamagnetic (ISP) scaling law. The red line in (b) represents the fit using the modified Langevin function, illustrating the presence of dipolar interactions among nanoparticles.

$\approx 1.034 \times 10^{-2}$  eV. Although specific reports on dipolar interaction energies in  $\text{MnFe}_2\text{O}_4$  are scarce, this value is comparable to those observed in magnetite ( $\text{Fe}_3\text{O}_4$ ) nanoparticles dispersed in polymeric matrices, such as photoreticulated PEGDA-600.<sup>110</sup> This supports the presence of moderate interparticle interactions in the studied  $\text{MnFe}_2\text{O}_4$  system. Consequently, the observed low coercivity and small squareness ratio can be ascribed to the combined effects of reduced magnetic anisotropy and notable dipolar interactions, both of which inhibit the alignment and stability of magnetic moments under an applied field.

## 4. Conclusion

In this study, we investigated the structural, optical, and magnetic properties of  $\text{CoFe}_2\text{O}_4$  and  $\text{MnFe}_2\text{O}_4$  nanoparticles synthesized *via* a green microwave-assisted co-precipitation method using coconut coir extract. Rietveld refinement of XRD data confirmed the formation of a single-phase cubic spinel structure with the  $Fd\bar{3}m$  space group in both samples. The refinement also revealed a mixed cation distribution, with  $\text{Co}^{2+}$  and  $\text{Mn}^{2+}$  ions occupying both tetrahedral (A) and octahedral (B) sites, indicative of a partially inverse spinel structure. This cation inversion was further supported by the presence of characteristic Raman doublets, a signature of structural disorder and mixed occupancy in ferrite nanocrystals. UV-vis analysis revealed direct optical bandgap energies of 2.66 eV for  $\text{CoFe}_2\text{O}_4$  and 2.64 eV for  $\text{MnFe}_2\text{O}_4$ . These values, along with the photoluminescence emission features and Urbach energies, were consistent with a proposed energy band diagram that accurately reflects the electronic transitions between crystal field-split states and defect-related levels in the spinel lattice. Mie theory analysis of the UV-vis absorption spectra provided insight into photothermal conversion efficiency, highlighting a dominant role of absorption in energy dissipation for  $\text{CoFe}_2\text{O}_4$ , whereas  $\text{MnFe}_2\text{O}_4$  showed a greater contribution from scattering due to larger particle size. Magnetic measurements

across varying temperatures revealed distinct behaviors between the two samples. For  $\text{CoFe}_2\text{O}_4$ , high coercivity and squareness ratio were attributed to strong surface spin anisotropy and magnetocrystalline effects. In contrast,  $\text{MnFe}_2\text{O}_4$  exhibited lower coercivity and squareness ratio, explained by weaker magnetic anisotropy and pronounced dipolar interactions. The temperature dependence of saturation magnetization followed Bloch's law, with extracted spin-wave constants aligning with previously reported values for ferrite systems. Analysis using the Stoner–Wohlfarth model, Kneller's law, and a modified Langevin function further confirmed that  $\text{CoFe}_2\text{O}_4$  behaves as a weakly interacting single-domain ferrimagnet, while  $\text{MnFe}_2\text{O}_4$  displays interacting superparamagnetic characteristics. Overall, these findings demonstrate that cation substitution, particle size, and surface-related effects play pivotal roles in governing the multifunctional properties of spinel ferrite nanoparticles, thereby establishing a robust basis for optimizing their performance in magnetic, photothermal, and optoelectronic applications.

## Author contributions

Tran Thi Ngoc Nha: investigation, synthesis samples, formal analysis, data curation. Shankar Hari Prakash: synthesis samples. Selvaraj Mohana Roopan and James Jebaseelan Samuel: supervision, review & editing and project administration. Dang Ngoc Toan: investigation, formal analysis. Dinh Thanh Khan and Do Danh Bich: investigation, formal analysis. Le Thi Tuyet Ngan: investigation, formal analysis. Tran Dang Thanh: conceptualization, investigation, formal analysis. Do Hung Manh and Pham Thanh Phong: conceptualization, investigation, formal analysis, data curation, writing-review & editing.

## Conflicts of interest

The authors declare that they have no conflict of interest.



## Data availability

The data that support the findings of this study are available within the article.

## Acknowledgements

Tran Thi Ngoc Nha was funded by the Master, PhD Scholarship Programme of Vingroup Innovation Foundation (VINIF), code VINIF.2024.TS.011.

## References

- S. C. Tolani, A. R. Golhar and K. G. Rewatkar, A review of morphological, structural behaviour and technological applications of ferrites, *AIP Conf. Proc.*, 2019, **2104**, 030032, DOI: [10.1063/1.5100459](https://doi.org/10.1063/1.5100459).
- A. I. Borhan, A. R. Iordan, M. N. Palamaru, and D. Ghercã, *Applications of Nanostructured Ferrites*, Woodhead Publishing Series in Electronic and Optical Materials, 2023, pp. 83–102, DOI: [10.1016/B978-0-443-18874-9.00003-5](https://doi.org/10.1016/B978-0-443-18874-9.00003-5).
- W. Wang, Z. Ding, X. Zhao, S. Wu, F. Li, M. Yue and J. Ping Liu, Microstructure and magnetic properties of  $\text{MFe}_2\text{O}_4$  (M = Co, Ni, and Mn) ferrite nanocrystals prepared using colloid mill and hydrothermal method, *J. Appl. Phys.*, 2015, **117**, 17A328, DOI: [10.1063/1.4917463](https://doi.org/10.1063/1.4917463).
- T. N. N. Tran, D. N. Toan, P. H. Nam, Do H. Manh, D. T. Khan and P. T. Phong, Determine elastic parameters and nanocrystalline size of spinel ferrites  $\text{MFe}_2\text{O}_4$  (M = Co, Fe, Mn, Zn) through X-ray diffraction and infrared spectrum: Comparative approach, *J. Alloys Compd.*, 2024, **996**, 174773, DOI: [10.1016/j.jallcom.2024.174773](https://doi.org/10.1016/j.jallcom.2024.174773).
- S. Chikazumi, *Physics of Ferromagnetism*, Chapter 9, Clarendon Press, Oxford, 1997, p. 199.
- D. T. Tran, T. T. N. Nha, T. T. Ha Giang, P. H. Nam, D. N. Toan, D. T. Khan, Do Hung Manh and P. Thanh Phong, Structural, optical, magnetic properties and energy-band structure of  $\text{MFe}_2\text{O}_4$  (M = Co, Fe, Mn) nanoferrites prepared by co-precipitation technique, *RSC Adv.*, 2024, **14**, 23645, DOI: [10.1039/d4ra04692g](https://doi.org/10.1039/d4ra04692g).
- S. Amiri and H. Shokrollahi, The role of cobalt ferrite magnetic nanoparticles in medical science, *Mater. Sci. Eng., C*, 2013, **33**, 1, DOI: [10.1016/j.msec.2012.09.003](https://doi.org/10.1016/j.msec.2012.09.003).
- N. Akhlaghi and G. Najafpour-Darzi, Manganese ferrite ( $\text{MnFe}_2\text{O}_4$ ) Nanoparticles: From synthesis to application -A review, *J. Ind. Eng. Chem.*, 2021, **103**, 292, DOI: [10.1016/j.jiec.2021.07.043](https://doi.org/10.1016/j.jiec.2021.07.043).
- D. K. Mondal, C. Borgohain, N. Paul and J. P. Borah, Tuning hyperthermia efficiency of  $\text{MnFe}_2\text{O}_4/\text{ZnS}$  nanocomposites by controlled ZnS concentration, *J. Mater. Res. Technol.*, 2019, **8**, 5659, DOI: [10.1016/j.jmrt.2019.09.034](https://doi.org/10.1016/j.jmrt.2019.09.034).
- X.-Yu Long, J.-Y. Lia, S. Dong and H.-Z. Lian, Spinel-type manganese ferrite ( $\text{MnFe}_2\text{O}_4$ ) microspheres: A novel affinity probe for selective and fast enrichment of phosphopeptides, *Talanta*, 2017, **166**, 36, DOI: [10.1016/j.talanta.2017.01.025](https://doi.org/10.1016/j.talanta.2017.01.025).
- F. H. Mohammadabadi, S. M. Masoudpanah, S. Alamolhoda and H. R. Koohdar, Electromagnetic microwave absorption properties of high entropy spinel ferrite  $((\text{MnNiCuZn})_{1-x}\text{Co}_x\text{Fe}_2\text{O}_4)/\text{graphene}$  nanocomposites, *J. Mater. Res. Technol.*, 2021, **14**, 1099, DOI: [10.1016/j.jmrt.2021.07](https://doi.org/10.1016/j.jmrt.2021.07).
- K. C. Das and S. S. Dhar, Rapid catalytic degradation of malachite green by  $\text{MgFe}_2\text{O}_4$  nanoparticles in presence of  $\text{H}_2\text{O}_2$ , *J. Alloys Compd.*, 2020, **828**, 154462, DOI: [10.1016/j.jallcom.2020.154462](https://doi.org/10.1016/j.jallcom.2020.154462).
- M. A. Mahdy, I. K. El Zawawi and M. M. Ahmad, Structure, optical and magnetic properties of  $\text{PVA}/\text{CuO}/\text{CoFe}_2\text{O}_4$  nanocomposite films for flexible magneto-electronic applications, *Mater. Sci. Eng., B*, 2024, **299**, 117028, DOI: [10.1016/j.mseb.2023.117028](https://doi.org/10.1016/j.mseb.2023.117028).
- P. B. Balakrishnan, N. Silvestri, T. Fernandez-Cabada, F. Marinaro, S. Fernandes, S. Fiorito, M. Miscuglio, D. Serantes, S. Ruta, K. Livesey and O. Hovorka, Exploiting unique alignment of cobalt ferrite nanoparticles, mild hyperthermia, and controlled intrinsic cobalt toxicity for cancer therapy, *Adv. Mater.*, 2020, **32**, 2003712, DOI: [10.1002/adma.202003712](https://doi.org/10.1002/adma.202003712).
- H. Zhang, Y. Guo, J. Jiao, Y. Qiu, Y. Miao, Y. He, Y. Z. Li, C. Xia, L. Li, J. Cai and K. Xu, A hepatocyte-targeting nanoparticle for enhanced hepatobiliary magnetic resonance imaging, *Nat. Biomed. Eng.*, 2023, **7**, 221, DOI: [10.1038/s41551-022-00975-2](https://doi.org/10.1038/s41551-022-00975-2).
- K. R. Sanchez-Lievanos, J. L. Stair and K. E. Knowles, Cation Distribution in Spinel Ferrite Nanocrystals: Characterization, Impact on their Physical Properties, and Opportunities for Synthetic Control, *Inorg. Chem.*, 2021, **60**, 4291, DOI: [10.1021/acs.inorgchem.1c00040](https://doi.org/10.1021/acs.inorgchem.1c00040).
- S. M. Ansari, A. Younis, Y. D. Kolekar and C. V. Ramana, Cobalt ferrite nanoparticles: The physics, synthesis, properties, and applications, *Appl. Phys. Rev.*, 2025, **12**, 021308, DOI: [10.1063/5.0244555](https://doi.org/10.1063/5.0244555).
- B. E. Kashevsky, V. E. Agabekov, S. B. Kashevsky, K. A. Kekalo, E. Yu. Manina, I. V. Prokhorov and V. S. Ulashchik, Study of cobalt ferrite nanosuspensions for low-frequency ferromagnetic hyperthermia, *Partic.*, 2008, **6**, 322, DOI: [10.1016/j.partic.2008.07.001](https://doi.org/10.1016/j.partic.2008.07.001).
- P. H. Nam, L. T. Lu, P. H. Linh, D. H. Manh, Le Thi Thanh Tam, N. X. Phuc and P. T. Phong, In-Ja Lee, Polymer-coated cobalt ferrite nanoparticles: synthesis, characterization, and toxicity for hyperthermia applications, *New J. Chem.*, 2018, **42**, 14530, DOI: [10.1039/C8NJ01701H](https://doi.org/10.1039/C8NJ01701H).
- P. T. Phong, N. X. Phuc, P. H. Nam, N. V. Chien, D. D. Dung and P. H. Linh, Size-controlled heating ability of  $\text{CoFe}_2\text{O}_4$  nanoparticles for hyperthermia applications, *Phys. B*, 2018, **531**, 30, DOI: [10.1016/j.physb.2017.12.010](https://doi.org/10.1016/j.physb.2017.12.010).
- J. K. Rajput and G. Kaur, Synthesis and applications of  $\text{CoFe}_2\text{O}_4$  nanoparticles for multicomponent reactions, *Catal. Sci. Technol.*, 2014, **4**, 142, DOI: [10.1039/C3CY00594A](https://doi.org/10.1039/C3CY00594A).
- G. Qi, H. Ren, H. Fan and Y. Liu, Preparation of  $\text{CoFe}_2\text{O}_4$  nanoparticles based on high-gravity technology and application for the removal of lead, *Chem. Eng. Res. Des.*, 2019, **147**, 520, DOI: [10.1016/j.cherd.2019.05.047](https://doi.org/10.1016/j.cherd.2019.05.047).



- 23 M. Ali, T. Pirhoushyaran and S. Hamid Esmaceli-Faraj, Synthesis of  $\text{CoFe}_2\text{O}_4$  magnetic nanoparticles for application in photocatalytic removal of azithromycin from waste water, *Sci. Rep.*, 2022, **12**, 19171, DOI: [10.1038/s41598-022-21231-2](https://doi.org/10.1038/s41598-022-21231-2).
- 24 A. M. Mohammad, H. Mehranfar, K. S. Rasol, M. M. Kareem, Y. H. Azeez and M. M. Mohammed, Temperature-dependence structural, morphological and magnetic properties of cobalt-cadmium ferrite nanoparticles: supported by theoretical study, *Bull. Mater. Sci.*, 2024, **47**, 24, DOI: [10.1007/s12034-023-03107-x](https://doi.org/10.1007/s12034-023-03107-x).
- 25 P. V. Chernozem, A. Urakova, D. A. Koptsev, M. A. Surmeneva, D. V. Wagner, E. Yu. Gerasimov, K. N. Romanyuk, A. L. Kholkin, R. V. Chernozem and R. A. Surmenev, Ultrafast *in situ* microwave-assisted hydrothermal synthesis of nanorods and soft magnetic colloidal nanoparticles based on  $\text{MnFe}_2\text{O}_4$ , *Ceram. Interfaces*, 2024, **50**, 17380, DOI: [10.1016/j.ceramint.2024.02.227](https://doi.org/10.1016/j.ceramint.2024.02.227).
- 26 F. Bayça, Characterization and magnetic properties of  $\text{CoFe}_2\text{O}_4$  nanoparticles synthesized by the co-precipitation method, *Int. J. Appl. Ceram. Technol.*, 2024, **21**, 544, DOI: [10.1111/ijac.14518](https://doi.org/10.1111/ijac.14518).
- 27 A. V. Ivanova, E. V. Ivanova, A. A. Nikitin, V. M. Cherepanov and M. A. Abakumov, Thermal decomposition of acetylacetonates for highly reproducible synthesis of M-ferrite (Mn, Co and Zn) nanoparticles with tunable magnetic properties, *J. Alloys Compd.*, 2024, **976**, 172737, DOI: [10.1016/j.jallcom.2023.172737](https://doi.org/10.1016/j.jallcom.2023.172737).
- 28 E. M. Boris, K. D. Panevalvan, M. L. Petrov, C. E. Céline, D. 'O. J.-L. Rehspringer and M. Kurmoo, Mechano-Synthesis, Characterization, and Magnetic Properties of Nanoparticles of Cobalt Ferrite,  $\text{CoFe}_2\text{O}_4$ , *Chem. Mater.*, 2004, **16**, 5689, DOI: [10.1021/cm049189u](https://doi.org/10.1021/cm049189u).
- 29 A. Lassoued, M. S. Lassoued and F. Karolak, Synthesis, structural, optical, morphological and magnetic characterization of copper substituted nickel ferrite ( $\text{Cu}_x\text{Ni}_{1-x}\text{Fe}_2\text{O}_4$ ) through co-precipitation method, *J. Mater. Sci.: Mater. Electron.*, 2017, **28**, 18480, DOI: [10.1007/s10854-017-7795-4](https://doi.org/10.1007/s10854-017-7795-4).
- 30 T. Tatarchuk, M. Bououdina, J. Judith Vijaya and L. John Kennedy, Spinel ferrite nanoparticles: Synthesis, crystal structure, properties, and perspective applications, *Springer Proc. Phys.*, 2017, **195**, 305, DOI: [10.1007/978-3-319-56422-7\\_22](https://doi.org/10.1007/978-3-319-56422-7_22).
- 31 M. Vadivel, R. R. Babu, M. Arivanandhan, K. Ramamurthi and Y. Hayakawa, Role of SDS surfactant concentrations on the structural, morphological, dielectric and magnetic properties of  $\text{CoFe}_2\text{O}_4$  nanoparticles, *RSC Adv.*, 2015, **5**, 27060, DOI: [10.1039/C5RA01162K](https://doi.org/10.1039/C5RA01162K).
- 32 B. Kharisov, O. Kharissova, and U. Ortiz-Mendez, Microwaves: Microwave-Assisted Hydrothermal Synthesis of Nanoparticles, *CRC Concise Encyclopedia of Nanotechnology*, CRC Press, Boca Raton, FL, USA, 2016, pp. 588–599.
- 33 S. Dichayal, V. Murade, S. Deshmukh, S. Pansambal, D. Hase and R. Oza, Green Synthesis of Cobalt Ferrite Nanoparticles: A Comprehensive Review on Eco-friendly Approaches, Characterization Techniques, and Potential Applications, *J. Chem. Rev.*, 2024, **6**, 514, DOI: [10.48309/JCR.2024.471812](https://doi.org/10.48309/JCR.2024.471812).
- 34 S. M. Roopan, S. M. Madhumitha, G. Rahuman, A. A. Kamaraj, C. Bharathi and A. Surendra, Low-cost and eco-friendly phyto-synthesis of silver nanoparticles using *Cocos nucifera* coir extract and its larvicidal activity, *Ind. Crops Prod.*, 2013, **43**, 631, DOI: [10.1016/j.indcrop.2012.08.013](https://doi.org/10.1016/j.indcrop.2012.08.013).
- 35 G. Elango and S. M. Roopan, Green synthesis, spectroscopic investigation and photocatalytic activity of lead nanoparticles, *Spectrochim. Acta, Part A*, 2015, **139**, 367, DOI: [10.1016/j.saa.2014.12.066](https://doi.org/10.1016/j.saa.2014.12.066).
- 36 G. Elango, S. M. Roopan, N. A. Al-Dhabi, M. V. Arasu, K. I. Damodharan and K. Elumalai, *Cocos nucifera* coir-mediated green synthesis of Pd NPs and its investigation against larvae and agricultural pest, *Artif. Cells, Nanomed., Biotechnol.*, 2017, **45**, 1581, DOI: [10.1080/21691401.2016.1262382](https://doi.org/10.1080/21691401.2016.1262382).
- 37 F. Rahman, Md A. M. Patwary, Md A. B. Siddique, M. S. Bashar, Md A. Haque, B. Akter, R. Rashid, Md A. Haque and A. K. M. Royhan Uddin, Green synthesis of zinc oxide nanoparticles using *Cocos nucifera* leaf extract: characterization, antimicrobial, antioxidant and photocatalytic activity, *R. Soc. Open Sci.*, 2022, **23**, 220858, DOI: [10.1098/rsos.220858](https://doi.org/10.1098/rsos.220858).
- 38 A. Vanangamudia and S. Punniyakoti, *Cocos nucifera*-mediated electrochemical synthesis and coating of CuO/ZnO nanostructures on Fe ship strips for marine application, *Green Chem. Lett. Rev.*, 2024, **17**, 2356612, DOI: [10.1080/17518253.2024.2356612](https://doi.org/10.1080/17518253.2024.2356612).
- 39 S. Yu, Q. Wang, Y. Chen, Y. Wang and J. Wang, Microwave-assisted synthesis of spinel ferrite nanospherolites, *Mater. Lett.*, 2020, **278**, 128431, DOI: [10.1016/j.matlet.2020.128431](https://doi.org/10.1016/j.matlet.2020.128431).
- 40 M. G. Idris, H. Y. Hafeez, J. Mohammed, A. B. Suleiman and C. E. Ndikilar, A review on recent development in the spinel ferrites-based materials for efficient solar fuel (hydrogen) generation via photocatalytic water-splitting, *Appl. Surf. Sci. Adv.*, 2023, **18**, 100468, DOI: [10.1016/j.apsadv.2023.100468](https://doi.org/10.1016/j.apsadv.2023.100468).
- 41 M. Madhukara Naik, H. J. Yashwanth, M. Vinuth, G. Nagaraju, K. Hareesh and H. S. B. Naik, Microwave radiation assisted synthesis of  $\text{NiFe}_2\text{O}_4\text{-CoFe}_2\text{O}_4$  nanocomposites for photocatalytic and photoelectrochemical water splitting applications, *Inorg. Chem. Commun.*, 2024, **160**, 111898, DOI: [10.1016/j.inoche.2023.111898](https://doi.org/10.1016/j.inoche.2023.111898).
- 42 H. Brian, Toby, R factors in Rietveld analysis: How good is good enough?, *Powder Diffr.*, 2006, **21**, 67, DOI: [10.1154/1.2179804](https://doi.org/10.1154/1.2179804).
- 43 T. R. Tatarchuk, M. Bououdina, N. D. Paliychuk, I. P. Yaremiy and V. V. Moklyak, Structural characterization and antistructure modeling of cobalt substituted zinc ferrites, *J. Alloys Compd.*, 2017, **694**, 777, DOI: [10.1016/j.jallcom.2016.10.067](https://doi.org/10.1016/j.jallcom.2016.10.067).



- 44 S. Jonak and J. P. Borah, Correlation between cation distribution and heating efficiency of annealed  $\text{Fe}_3\text{O}_4$  nanoparticles, *Mater. Today Commun.*, 2021, **26**, 101789, DOI: [10.1016/j.mtcomm.2020.101789](https://doi.org/10.1016/j.mtcomm.2020.101789).
- 45 R. D. Shannon, Revised Effective Ionic Radii and Systematic Studies of Interatomic Distances in Halides and Chalcogenides, *Acta Crystallogr. Sect. A Cryst. Phys. Diffraction. Gen. Crystallogr.*, 1976, **32**, 751, DOI: [10.1107/S0567739476001551](https://doi.org/10.1107/S0567739476001551).
- 46 A. V. Ravindra, M. Chandrika, Ch. Rajesh, P. Kollu, S. Ju and S. D. Ramarao, Simple synthesis, structural and optical properties of cobalt ferrite nanoparticles, *Eur. Phys. J. Plus*, 2019, **134**, 296, DOI: [10.1140/epjp/i2019-12690-2](https://doi.org/10.1140/epjp/i2019-12690-2).
- 47 S. P. Yadav, S. S. Shinde, P. Bhatt, S. S. Meena and K. Y. Rajpure, Distribution of cations in  $\text{Co}_{1-x}\text{Mn}_x\text{Fe}_2\text{O}_4$  using XRD, magnetization and Mossbauer spectroscopy, *J. Alloys Compd.*, 2015, **646**, 550, DOI: [10.1016/j.jallcom.2015.05.270](https://doi.org/10.1016/j.jallcom.2015.05.270).
- 48 Z. K. Heiba, M. Bakr Mohamed, M. A. Ahmed, M. A. A. Moussa and H. H. Hamdeh, Cation distribution and dielectric properties of nanocrystalline gallium substituted nickel ferrite, *J. Alloys Compd.*, 2014, **586**, 773, DOI: [10.1016/j.jallcom.2013.10.137](https://doi.org/10.1016/j.jallcom.2013.10.137).
- 49 S. M. Patange, S. E. Shirsath, S. S. Jadhav and K. M. Jadhav, Cation distribution study of nanocrystalline  $\text{NiFe}_{2-x}\text{Cr}_x\text{O}_4$  ferrite by XRD, magnetization and Mossbauer spectroscopy, *Phys. Status Solidi A*, 2012, **209**, 347, DOI: [10.1002/pssa.201127232](https://doi.org/10.1002/pssa.201127232).
- 50 S. Deshpande, S. Patil, S. Kuchibhatla and S. Seal, Size dependency variation in lattice parameter and valency states in nanocrystalline ceriumoxide, *Appl. Phys. Lett.*, 2005, **87**, 133113, DOI: [10.1063/1.2061873](https://doi.org/10.1063/1.2061873).
- 51 M. M. L. Sonia, S. Anand, V. M. Vinose, M. A. Janifer, S. Pauline and A. Manikandan, Effect of lattice strain on structure, morphology and magneto-dielectric properties of spinel  $\text{NiGd}_x\text{Fe}_{2-x}\text{O}_4$  ferrite nano-crystallites synthesized by sol-gel route, *J. Magn. Magn. Mater.*, 2018, **466**, 238, DOI: [10.1016/j.jmmm.2018.07.017](https://doi.org/10.1016/j.jmmm.2018.07.017).
- 52 V. Kumar, A. Rana, M. S. Yadav and R. P. Pant, Size-induced effect on nano-crystalline  $\text{CoFe}_2\text{O}_4$ , *J. Magn. Magn. Mater.*, 2008, **320**, 1729, DOI: [10.1016/j.jmmm.2008.01.021](https://doi.org/10.1016/j.jmmm.2008.01.021).
- 53 R. Kumar and M. Kar, Correlation between lattice strain and magnetic behavior in non-magnetic Ca substituted nano-crystalline cobalt ferrite, *Ceram. Interfaces*, 2016, **42**, 6640, DOI: [10.1016/j.ceramint.2016.01.007](https://doi.org/10.1016/j.ceramint.2016.01.007).
- 54 B. Albin, *Raman Spectroscopy and Nanostructured Complex Systems: A Satisfactory Win to Win Game?*, University of Pavia, Pavia, 2021.
- 55 T. Yu, Z. X. Shen, Y. Shi and J. Ding, Cation migration and magnetic ordering in spinel  $\text{CoFe}_2\text{O}_4$ : micro-Raman scattering study, *J. Phys.: Condens. Matter*, 2002, **14**, L613, DOI: [10.1088/0953-8984/14/37/101](https://doi.org/10.1088/0953-8984/14/37/101).
- 56 W. Wang, Z. Ding, X. Zhao, S. Wu, F. Li, M. Yue and J. Ping Liu, Microstructure and magnetic properties of  $\text{MFe}_2\text{O}_4$  (M= Co, Ni, and Mn) ferrite nanocrystals prepared using colloid mill and hydrothermal method, *J. Appl. Phys.*, 2015, **117**, 17A328, DOI: [10.1063/1.4917463](https://doi.org/10.1063/1.4917463).
- 57 Z. Z. Lazarevic, C. Jovalekic, A. Milutinovic, D. Sekulic, V. N. Ivanovski, A. Recnik, B. Cekic and N. Z. Romcevic, Nanodimensional spinel  $\text{NiFe}_2\text{O}_4$  and  $\text{ZnFe}_2\text{O}_4$  ferrites prepared by soft mechanochemical synthesis, *J. Appl. Phys.*, 2013, **113**, 187221, DOI: [10.1063/1.4801962](https://doi.org/10.1063/1.4801962).
- 58 M. H. Sousa, F. A. Tourinho and J. C. Rubim, Use of Raman micro-spectroscopy in the characterization of  $\text{M}^{\text{II}}\text{Fe}_2\text{O}_4$  (M = Fe, Zn) electric double layer ferrofluids, *J. Raman Spectrosc.*, 2000, **31**, 185, DOI: [10.1002/\(SICI\)1097-4555\(200003](https://doi.org/10.1002/(SICI)1097-4555(200003).
- 59 A. Ahlawat and V. G. Sathe, Raman study of  $\text{NiFe}_2\text{O}_4$  nanoparticles, bulk and films: effect of laser power, *J. Raman Spectrosc.*, 2011, **42**, 1087, DOI: [10.1002/jrs.2791](https://doi.org/10.1002/jrs.2791).
- 60 R. G. Burns, *Mineralogical Applications of Crystal Field Theory*, Cambridge University Press, Cambridge, 1993.
- 61 S. M. Ansari, V. Kashid, H. Salunke, D. Sen, Y. D. Kolekar and C. Ramana, First-principles calculations of the electronic structure and magnetism of nanostructured  $\text{CoFe}_2\text{O}_4$  microgranules and nanoparticles, *Phys. Rev. B*, 2020, **102**, 035446, DOI: [10.1103/PhysRevB.102.035446](https://doi.org/10.1103/PhysRevB.102.035446).
- 62 J. Tauc, Optical properties and electronic structure of amorphous Ge and Si, *Mater. Res. Bull.*, 1968, **3**, 37, DOI: [10.1016/0025-5408\(68\)90023-8](https://doi.org/10.1016/0025-5408(68)90023-8).
- 63 S. M. Ansari, D. Phase, Y. D. Kolekar and C. V. Ramana, Effect of Manganese-Doping on the chemical and optical properties of cobalt ferrite nanoparticles, *Mater. Sci. Eng., B*, 2024, **300**, 117134, DOI: [10.1016/j.mseb.2023.117134](https://doi.org/10.1016/j.mseb.2023.117134).
- 64 M. Sundararajan, L. John Kennedy, J. Judith Vijaya and U. Aruldoss, Microwave combustion synthesis of  $\text{Co}_{1-x}\text{Zn}_x\text{Fe}_2\text{O}_4$  ( $0 \leq x \leq 0.5$ ): structural, magnetic, optical and vibrational spectroscopic studies, *Spectrochim. Acta, Part A*, 2015, **140**, 421, DOI: [10.1016/j.saa.2014.12.035](https://doi.org/10.1016/j.saa.2014.12.035).
- 65 M. A. Shilpa Amulya, H. P. Nagaswarupa, M. R. Anil Kumar, C. R. Ravikumar and K. B. Kusuma, Sonochemical synthesis of  $\text{MnFe}_2\text{O}_4$  nanoparticles and their electrochemical and photocatalytic properties, *J. Phys. Chem. Solids*, 2021, **148**, 109661, DOI: [10.1016/j.jpcs.2020.109661](https://doi.org/10.1016/j.jpcs.2020.109661).
- 66 S. M. Wasim, C. Rincon, G. Marin, P. Bocaranda, E. Hernandez, I. Bonalde and E. Medina, Effect of structural disorder on the Urbach energy in Cu ternaries, *Phys. Rev. B:Condens. Matter Mater. Phys.*, 2001, **64**, 195101, DOI: [10.1103/PhysRevB.64.195101](https://doi.org/10.1103/PhysRevB.64.195101).
- 67 V. R. Akshay, B. Arun, G. Mandal and M. Vasundhara, Visible range optical absorption, Urbach energy estimation and paramagnetic response in Cr-doped  $\text{TiO}_2$  nanocrystals derived by a sol-gel method, *Phys. Chem. Chem. Phys.*, 2019, **21**, 12991, DOI: [10.1039/c9cp01351b](https://doi.org/10.1039/c9cp01351b).
- 68 H. Hussein, S. S. Ibrahim and S. A. Khairy, Eco-friendly  $\text{CoFe}_2\text{O}_4$  ferrite nanoparticles prepared using greek yogurt solution: deep insights into optical properties and abnormal semiconductor-insulator-semiconductor transitions for optoelectronics and catalytic applications, *Mater. Adv.*, 2025, **6**, 2297–2327, DOI: [10.1039/D4MA01172D](https://doi.org/10.1039/D4MA01172D).
- 69 M. E. Sadat, M. K. Baghbador, A. W. Dunn, H. P. Wagner, R. C. Ewing, J. Zhang, H. Xu, G. M. Pauletti, D. B. Mast and D. Shi, Photoluminescence and photothermal effect



- of Fe<sub>3</sub>O<sub>4</sub> nanoparticles for medical imaging and therapy, *Appl. Phys. Lett.*, 2014, **105**, 091903, DOI: [10.1063/1.4895133](https://doi.org/10.1063/1.4895133).
- 70 S. K. Paswan, S. Kumari, M. Kar, A. Singh, H. Pathak, J. P. Borah and L. Kumar, Optimization of structure-property relationships in nickel ferrite nanoparticles annealed at different temperature, *J. Phys. Chem. Solids*, 2021, **151**, 109928, DOI: [10.1016/j.jpics.2020.109928](https://doi.org/10.1016/j.jpics.2020.109928).
- 71 B. Sreematha, N. Arundhathi and D. Ravinder, Influence of Cerium substitution on structural, optical, and electrical transport properties of Ni-Nano ferrites prepared by Citrate gel auto combustion method, *Results Chem.*, 2023, **5**, 100929, DOI: [10.1016/j.rechem.2023.100929](https://doi.org/10.1016/j.rechem.2023.100929).
- 72 R. Bhargava, P. K. Sharma, R. K. Dutta, S. Kumar, A. C. Pandey and N. Kumar, Influence of Co-doping on the thermal, structural, and optical properties of sol-gel derived ZnO nanoparticles, *Mater. Chem. Phys.*, 2010, **120**, 393, DOI: [10.1016/j.matchemphys.2009.11.024](https://doi.org/10.1016/j.matchemphys.2009.11.024).
- 73 S. Tongay, J. Suh, C. Ataca, F. Wen, A. Luce, J. S. Kang, J. Liu, C. Ko, R. Raghunathanan, J. Zhou, F. Ogletree, J. Li, J. C. Grossman and J. Wu, Defects activated photoluminescence in two-dimensional semiconductors: interplay between bound, charged and free excitons, *Sci. Rep.*, 2013, **3**, 2657, DOI: [10.1038/srep02657](https://doi.org/10.1038/srep02657).
- 74 K. J. Kim, H. S. Lee, M. H. Lee and S. Ho Lee, Comparative magneto-optical investigation of d-d charge-transfer transitions in Fe<sub>3</sub>O<sub>4</sub>, CoFe<sub>2</sub>O<sub>4</sub>, and NiFe<sub>2</sub>O<sub>4</sub>, *J. Appl. Phys.*, 2002, **91**, 9974, DOI: [10.1063/1.1480482](https://doi.org/10.1063/1.1480482).
- 75 W. F. J. Fontijn, P. J. van der Zaag, N. F. Feiner, R. Metselaar and M. A. C. Devillers, A consistent interpretation of the magneto-optical spectra of spinel type ferrites (invited), *J. Appl. Phys.*, 1999, **85**, 5100, DOI: [10.1063/1.369091](https://doi.org/10.1063/1.369091).
- 76 D. L. Camphausen, J. M. D. Coey and B. K. Chakraverty, One Electron Energy Levels in Fe<sub>3</sub>O<sub>4</sub>, *Phys. Rev. Lett.*, 1972, **29**, 657, DOI: [10.1103/PhysRevLett.29.657](https://doi.org/10.1103/PhysRevLett.29.657).
- 77 C. Boxall, G. Kelsall and Z. Zhang, Photoelectrophoresis of colloidal iron oxides Part 2. Magnetite (Fe<sub>3</sub>O<sub>4</sub>), *J. Chem. Soc., Faraday Trans.*, 1996, **92**, 791, DOI: [10.1039/FT9969200791](https://doi.org/10.1039/FT9969200791).
- 78 S. F. Alvarado, M. Erbudak and P. Munz, Final-state effects in the 3d photoelectron spectrum of Fe<sub>3</sub>O<sub>4</sub> and comparison with Fe<sub>x</sub>O, *Phys. Rev. B*, 1976, **14**, 2740, DOI: [10.1103/PhysRevB.14.2740](https://doi.org/10.1103/PhysRevB.14.2740).
- 79 E. Fantechi, G. Campo, D. Carta, A. Corrias, C. de Julian Fernandez, D. Gatteschi, C. Innocenti, F. Pineider, F. Rugi and C. Sangregorio, Exploring the Effect of Co Doping in Fine Maghemite Nanoparticles, *J. Phys. Chem. C*, 2012, **116**, 8261, DOI: [10.1021/jp300806j](https://doi.org/10.1021/jp300806j).
- 80 R. Papalardo, P. L. Wood and R. C. Lineares Jr, Optical Absorption Study of Co-Doped Oxide Systems. II, *J. Chem. Phys.*, 1961, **35**, 2041, DOI: [10.1063/1.1732208](https://doi.org/10.1063/1.1732208).
- 81 Y. Zhao, M. E. Sadat, A. Dunna, H. Xu, C.-H. Chen, W. Nakasuga, R. C. Ewing and D. Shi, Photothermal effect on Fe<sub>3</sub>O<sub>4</sub> nanoparticles irradiated by white-light for energy-efficient window applications, *Sol. Energy Mater. Sol. Cells*, 2017, **161**, 247, DOI: [10.1016/j.solmat.2016.11.039](https://doi.org/10.1016/j.solmat.2016.11.039).
- 82 J. Zaanen, G. A. Sawatzky and J. W. Allen, Band gaps and electronic structure of transition-metal compounds, *Phys. Rev. Lett.*, 1985, **55**, 418, DOI: [10.1103/PhysRevLett.55.418](https://doi.org/10.1103/PhysRevLett.55.418).
- 83 B. S. Holinsworth, D. Mazumdar, H. Sims, Q.-C. Sun, M. K. Yurtisigi, S. K. Sarker, A. Gupta, W. H. Butler and J. L. Musfeldt, Chemical tuning of the optical band gap in spinel ferrites: CoFe<sub>2</sub>O<sub>4</sub> vs. NiFe<sub>2</sub>O<sub>4</sub>, *Appl. Phys. Lett.*, 2013, **103**, 082406, DOI: [10.1063/1.4818315](https://doi.org/10.1063/1.4818315).
- 84 T. A. C. Ulpe, K. C. L. Bauerfeind and T. Bredow, Influence of Spin State and Cation Distribution on Stability and Electronic Properties of Ternary Transition-Metal Oxides, *ACS Omega*, 2019, **4**, 4138, DOI: [10.1021/acsomega.8b03254](https://doi.org/10.1021/acsomega.8b03254).
- 85 A. Elfalaky and S. Soliman, Theoretical investigation of MnFe<sub>2</sub>O<sub>4</sub>, *J. Alloys Compd.*, 2013, **580**, 401, DOI: [10.1016/j.jallcom.2013.05.197](https://doi.org/10.1016/j.jallcom.2013.05.197).
- 86 S. Akhtar, A. Hussain, S. Noreen, N. Bibi, M. B. Tahir and J. U. Rehman, A comparative DFT study of MgFe<sub>2</sub>O<sub>4</sub> and MnFe<sub>2</sub>O<sub>4</sub> spinel ferrites at various pressures to investigate the structural, mechanical, electronic, magnetic and optical properties for multifunctional applications, *Comput. Theor. Chem.*, 2024, **1235**, 114546, DOI: [10.1016/j.comptc.2024.114546](https://doi.org/10.1016/j.comptc.2024.114546).
- 87 S. Sharifi, K. Rahimi and A. Yazdani, Highly improved supercapacitance properties of MnFe<sub>2</sub>O<sub>4</sub> nanoparticles by MoS<sub>2</sub> nanosheets, *Sci. Rep.*, 2021, **11**, 8378, DOI: [10.1038/s41598-021-87823-6](https://doi.org/10.1038/s41598-021-87823-6).
- 88 N. M. Refat, M. Y. Nassar and S. A. Sadeek, A controllable one-pot hydrothermal synthesis of spherical cobalt ferrite nanoparticles: synthesis, characterization, and optical properties, *RSC Adv.*, 2022, **12**, 25081, DOI: [10.1039/D2RA03345C](https://doi.org/10.1039/D2RA03345C).
- 89 T. T. D. Nguyen, M. F. Lin and W. D. Hsu, Investigations on electronic, magnetic, and optical properties of MnFe<sub>2</sub>O<sub>4</sub> through first-principles calculations, *Comput. Mater. Sci.*, 2024, **235**, 112831, DOI: [10.1016/j.commatsci.2024.112831](https://doi.org/10.1016/j.commatsci.2024.112831).
- 90 P. Laven, MiePlot, <http://www.philiplaven.com/mieplot.htm>.
- 91 R. Grossinger, A critical examination of the law of approach to saturation, *Phys. Status Solidi A*, 1981, **66**, 665, DOI: [10.1002/pssa.2210660231](https://doi.org/10.1002/pssa.2210660231).
- 92 K. M. Krishnan, *Fundamentals and Applications of Magnetic Materials*, Oxford University Press, 1st edn, 2016.
- 93 S. T. Xua, Y. Q. Ma, G. H. Zheng and Z. X. Dai, Simultaneous effects of surface spins: rarely large coercivity, high remanence magnetization and jumps in the hysteresis loops observed in CoFe<sub>2</sub>O<sub>4</sub> nanoparticles, *Nanoscale*, 2015, **7**, 6520, DOI: [10.1039/C5NR00582E](https://doi.org/10.1039/C5NR00582E).
- 94 B. Aslibeiki, P. Kameli and H. Salamati, The effect of dipole-dipole interactions on coercivity, anisotropy constant, and blocking temperature of MnFe<sub>2</sub>O<sub>4</sub> nanoparticles, *J. Appl. Phys.*, 2016, **119**, 063901, DOI: [10.1063/1.4941388](https://doi.org/10.1063/1.4941388).
- 95 Y. Kumar, A. Sharma and P. M. Shirage, Impact of different morphologies of CoFe<sub>2</sub>O<sub>4</sub> nanoparticles for tuning of structural, optical and magnetic properties, *J. Alloys Compd.*, 2019, **778**, 398, DOI: [10.1016/j.jallcom.2018.11.128](https://doi.org/10.1016/j.jallcom.2018.11.128).



- 96 E. C. Stoner and E. P. Wohlfarth, A Mechanism of Magnetic Hysteresis in Heterogeneous Alloys, *Philos. Trans. R. Soc., A*, 1948, **240**, 599, DOI: [10.1098/rsta.1948.0007](https://doi.org/10.1098/rsta.1948.0007).
- 97 C. Kittle, *Introduction Solid State Physics*, John Wiley & Sons, 8th edn, 2004.
- 98 A. Franco Jr, F. L. A. Machado and V. S. Zapf, Magnetic properties of nanoparticles of cobalt ferrite at high magnetic field, *J. Appl. Phys.*, 2011, **110**, 053913, DOI: [10.1063/1.3626931](https://doi.org/10.1063/1.3626931).
- 99 Y. Yafet and C. Kittel, Antiferromagnetic Arrangements in Ferrites, *Phys. Rev.*, 1952, **87**, 290, DOI: [10.1103/PhysRev.87.290](https://doi.org/10.1103/PhysRev.87.290).
- 100 C. N. Chinnasamy, B. Jeyadevan, K. Shinoda, K. Tohji, D. J. Djayaprawira, M. Takahashi, R. Justin Joseyphus and A. Narayanasamy, Unusually high coercivity and critical single-domain size of nearly monodispersed CoFe<sub>2</sub>O<sub>4</sub> nanoparticles, *Appl. Phys. Lett.*, 2003, **83**, 2862, DOI: [10.1063/1.1616655](https://doi.org/10.1063/1.1616655).
- 101 D. Pal, M. Mandal, A. Chaudhuri, B. Das, D. Sarkar and K. Mandal, Micelles induced high coercivity in single domain cobalt-ferrite nanoparticles, *J. Appl. Phys.*, 2010, **108**, 124317, DOI: [10.1063/1.1616655](https://doi.org/10.1063/1.1616655).
- 102 U. Kurtan, R. Topkaya, A. Baykal and M. S. Toprak, Temperature dependent magnetic properties of CoFe<sub>2</sub>O<sub>4</sub>/CTAB nanocomposite synthesized by sol-gel auto-combustion technique, *Ceram. Interfaces*, 2013, **39**, 6551, DOI: [10.1016/j.ceramint.2013.01.088](https://doi.org/10.1016/j.ceramint.2013.01.088).
- 103 I. P. Muthuselvam and R. N. Bhowmik, Mechanical alloyed Ho<sup>3+</sup> doping in CoFe<sub>2</sub>O<sub>4</sub> spinel ferrite and understanding of magnetic nanodomains, *J. Magn. Magn. Mater.*, 2010, **322**, 767, DOI: [10.1016/j.jmmm.2009.10.057](https://doi.org/10.1016/j.jmmm.2009.10.057).
- 104 S. T. Xua, Y. Q. Ma, G. H. Zheng and Z. X. Dai, Simultaneous effects of surface spins: rarely large coercivity, high remanence magnetization and jumps in the hysteresis loops observed in CoFe<sub>2</sub>O<sub>4</sub> nanoparticles, *Nanoscale*, 2015, **7**, 6520, DOI: [10.1039/C5NR00582E](https://doi.org/10.1039/C5NR00582E).
- 105 E. F. Kneller and F. E. Luborsky, Particle Size Dependence of Coercivity and Remanence of Single-Domain Particles, *J. Appl. Phys.*, 1963, **34**, 656, DOI: [10.1063/1.1729324](https://doi.org/10.1063/1.1729324).
- 106 D. Pal, M. Mandal, A. Chaudhuri, B. Das, D. Sarkar and K. Mandal, Micelles induced high coercivity in single domain cobalt-ferrite nanoparticles, *J. Appl. Phys.*, 2010, **108**, 124317, DOI: [10.1063/1.3525994](https://doi.org/10.1063/1.3525994).
- 107 R. N. Bhowmik, V. Vasanthi and A. Poddar, Alloying of Fe<sub>3</sub>O<sub>4</sub> and Co<sub>3</sub>O<sub>4</sub> to develop Co<sub>3x</sub>Fe<sub>3(1-x)</sub>O<sub>4</sub> ferrite with high magnetic squareness, tunable ferromagnetic parameters, and exchange bias, *J. Alloys Compd.*, 2013, **578**, 585–594, DOI: [10.1016/j.jallcom.2013.06.160](https://doi.org/10.1016/j.jallcom.2013.06.160).
- 108 S. Verma and D. Pravarthana, One-Pot Synthesis of Highly Monodispersed Ferrite Nanocrystals: Surface Characterization and Magnetic Properties, *Langmuir*, 2011, **27**, 13189–13197, DOI: [10.1021/la202394n](https://doi.org/10.1021/la202394n).
- 109 M. Vasilakaki, K. N. Trohidou, D. Peddis, D. Fiorani, R. Mathieu, M. Hudl, P. Nordblad, C. Binns and S. Baker, Memory effects on the magnetic behavior of assemblies of nanoparticles with ferromagnetic core/antiferromagnetic shell morphology, *Phys. Rev. B:Condens. Matter Mater. Phys.*, 2013, **88**, 140402, DOI: [10.1103/PhysRevB.88.140402](https://doi.org/10.1103/PhysRevB.88.140402).
- 110 P. Allia, P. Tiberto, M. Coisson, A. Chiolerio, F. Celegato, F. Vinai, M. Sangermano, L. Suber and G. Marchegiani, Evidence for magnetic interactions among magnetite nanoparticles dispersed in photoreticulated PEGDA-600 matrix, *J. Nanopart. Res.*, 2011, **13**, 5615, DOI: [10.1007/s11051-011-0249-7](https://doi.org/10.1007/s11051-011-0249-7).

